

Axisymmetric collapse simulations of rotating massive stellar cores in full general relativity: Numerical study for prompt black hole formation

Yu-ichirou Sekiguchi and Masaru Shibata

Graduate School of Arts and Sciences, University of Tokyo, Tokyo, 153-8902, Japan

(Received 6 January 2005; published 18 April 2005)

We perform axisymmetric simulations for gravitational collapse of a massive iron core to a black hole in full general relativity. The iron cores are modeled by $\Gamma = 4/3$ equilibrium polytrope for simplicity. The hydrodynamic equations are solved using a high-resolution shock-capturing scheme with a parametric equation of state. The Cartoon method is adopted for solving the Einstein equations. Simulations are performed for a wide variety of initial conditions changing the mass ($\approx 2.0\text{--}3.0M_{\odot}$), the angular momentum, the rotational velocity profile of the core, and the parameters of the equations of state which are chosen so that the maximum mass of the cold spherical polytrope is $\approx 1.6M_{\odot}$. Then, the criterion for the prompt black hole formation is clarified in terms of the mass and the angular momentum for several rotational velocity profile of the core and equations of state. It is found that (i) with the increase of the thermal energy generated by shocks, the threshold mass for the prompt black hole formation is increased by 20–40%, (ii) the rotational centrifugal force increases the threshold mass by $\lesssim 25\%$, (iii) with the increase of the degree of differential rotation, the threshold mass is also increased, and (iv) the amplification factors shown in the results (i)–(iii) depend sensitively on the equation of state. We also find that the collapse dynamics and the structure of the shock formed at the bounce depend strongly on the stiffness of the adopted equation of state. In particular, as a new feature, a strong bipolar explosion is observed for the collapse of rapidly rotating iron cores with an equation of state which is stiff in subnuclear density and soft in supranuclear density. Gravitational waves are computed in terms of a quadrupole formula. It is also found that the waveform depends sensitively on the equations of state.

DOI: 10.1103/PhysRevD.71.084013

PACS numbers: 04.25.Dm, 04.30.-w, 04.40.Dg

I. INTRODUCTION

The black hole is one of the most striking and intriguing objects predicted in general relativity. A wide variety of recent observations have shown that black holes actually exist in the universe [1]. Among several types of the black holes, the existence of the stellar-mass black holes has been tightly confirmed. So far, about 20 stellar-mass black holes for which the mass is determined within a fairly small error have been observed in binary systems of our Galaxy and the large magellanic clouds [2]. Such black holes are believed to be formed from the stellar core collapse of massive stars. This fact stimulates the theoretical study for clarifying the physics of gravitational collapse and formation mechanism of the stellar-mass black holes. The formation of the black hole through the gravitational collapse is a highly nonlinear and dynamical phenomena. Therefore, numerical simulation in full general relativity is the unique approach to this problem.

Realistic simulations for the formation of stellar-mass black holes in massive rotating stellar core collapse is also increasingly important due to its possible association with gamma-ray bursts [3]. Recent observations have indicated that at least long-duration gamma-ray bursts are of cosmological origin [4] and associated with rotating stellar core collapse [5,6], probably to a black hole surrounded by a massive disk as suggested by [7–9]. Recent numerical analyses have also shown that if a progenitor of the collapse is massive and the angular momentum is large enough, a black hole surrounded by a massive disk will

be indeed formed [10–12]. However detailed simulations have not yet been done.

Stellar-mass black holes can be formed through the gravitational collapse of a degenerate iron core in excess of the Chandrasekhar mass [13,14]. It is well known that stars whose initial mass are larger than $\approx 10M_{\odot}$ evolve to form a core mainly composed of iron group elements [14]. Since the iron is the most stable nuclei and it does not generate energy by nuclear burning, the iron core contracts gradually. Accordingly, the central temperature, T_c , and central density, ρ_c , rise to be $T_c \gtrsim 10^{10}$ K and $\rho_c > 10^9$ g/cm³, resulting in the photo-dissociation of iron to lighter elements and subsequent electron capture that reduce the entropy of electrons. As a result, the adiabatic index Γ_s decreases below 4/3 and the iron core is destabilized to collapse. If the mass of the iron core is much larger than the maximum neutron star mass, a black hole will be formed soon after the collapse. However, the threshold mass of the iron core for prompt formation of a black hole has not been clarified yet. Note that due to the contribution of the thermal pressure and rotation, the iron core can be much larger than the maximum allowed neutron star mass of $\sim 2M_{\odot}$ for a sufficiently massive and rotating star.

Since massive stars in nature are rapidly rotating in general [15], it is necessary to explore the gravitational collapse of a rotating star in full general relativity for clarifying the black hole formation. Since Nakamura [16] and his collaborators [17] first presented a series of preliminary numerical simulations, a number of simulations for rotating stellar collapse to a black hole have been

performed in full general relativity [18–23]. However, the initial conditions and equations of state in the previous works are not very realistic for modeling the stellar core collapse. Thus, the simulations with a realistic setting remain to be an unsolved issue in general relativity.

Realistic simulations of rotating stellar core collapse have been performed intensively in the framework of Newtonian gravity [24–33]. Most of these studies mainly aim at clarifying the effect of the rotation on the dynamics of *neutron star formation* and gravitational waveforms from it. In particular, a comprehensive parameter study sweeping through various values of the stiffness of a parametric equation of state as well as rotational parameters was performed in [29]. It was shown that the dynamics of the collapse and resulting gravitational waveforms depend strongly not only on rotation but also on the stiffness of equations of state. Dimmelmeier *et al.* [34] extended the aforementioned study to general relativistic case using a conformal flatness formalism [35]. Fully general relativistic numerical studies of neutron star formation have been recently performed [36,37]. As shown in [34,36], the general relativistic effects significantly modify the dynamics of the collapse even in the formation of neutron stars.

Taking into account the present status described above, in this paper, we study a criterion for prompt black hole formation in the iron core collapse performing fully general relativistic simulations. The iron cores are modeled by $\Gamma = 4/3$ polytropes in equilibrium for simplicity. The major purpose of this paper is to clarify the threshold mass of the iron core for the prompt black hole formation and its dependence on the angular momentum, the rotational velocity profiles of the iron core, and the equations of state. To clarify the dependence on the equations of state in a clear manner, we adopt a parametric equation of state following previous papers [36,38].

The simulations are performed assuming that the collapse proceeds in an axisymmetric manner. This assumption is reasonable as far as the progenitor of the collapse is not very rapidly and highly differentially rotating (e.g., [38]). In this paper, we do not adopt such progenitor that are likely to be dynamical unstable against nonaxisymmetric deformation (cf. Sec. IV D 2 for discussion). Although for several models, the rotational kinetic energy is so large that the outcome formed in the collapse may be secularly unstable against nonaxisymmetric deformation, the secular time scale is much longer than the dynamical time scale of the core collapse. Hence, the collapse will proceed in an approximately axisymmetric manner in the time scale of interest. On the other hand, rapidly and differentially rotating stellar core collapse has to be studied in the three-dimensional simulation. Such simulation was recently performed and the detailed results are shown in a companion paper [38].

This paper is organized as follows. In Sec. II, we briefly review our formulation for general relativistic hydrody-

namical simulations, equations of state, and a quadrupole formula adopted in the present paper. In Sec. III, we describe the initial conditions. A detail of computational setting is also described. Sec. IV presents the numerical results, emphasizing the threshold mass for the prompt black hole formation and its dependence on the angular momentum and the adopted equations of state. Gravitational waveforms emitted in the neutron star formation are also shown. Sec. V is devoted to a summary. Throughout the paper, we adopt the geometrical units $G = c = 1$ where G and c are the gravitational constant and speed of light, respectively. The Latin indices i, j, k, \dots denote the spatial components of $x, y,$ and $z,$ and the Greek indices μ, \dots denote the spacetime components.

II. NUMERICAL IMPLEMENTATION

A. Brief summary of formulation and numerical method

We perform fully general relativistic simulations for rotating stellar core collapse in axial symmetry using the same formulation and numerical method as those presented in [39], to which the reader may refer for details of basic equations and successful test simulations.

In the $3 + 1$ formulation, the metric can be written in the form

$$ds^2 = (-\alpha^2 + \beta_k \beta^k) dt^2 + 2\beta_k dt dx^k + \gamma_{ij} dx^i dx^j, \quad (1)$$

where $\alpha, \beta^k,$ and γ_{ij} are the lapse function, the shift vector and metric in 3D spatial hypersurface, respectively. The extrinsic curvature is defined by

$$(\partial_t - \mathcal{L}_\beta)\gamma_{ij} = -2\alpha K_{ij}, \quad (2)$$

where \mathcal{L}_β is the Lie derivative with respect to β^k .

As in the series of our papers, we evolve $\phi \equiv \log(\det \gamma_{ij})/12,$ $\tilde{\gamma}_{ij} \equiv e^{-4\phi} \gamma_{ij},$ $\tilde{A}_{ij} \equiv e^{-4\phi} (K_{ij} - \gamma_{ij} K_k^k),$ and trace of the extrinsic curvature K_k^k together with three auxiliary functions $F_i \equiv \delta^{jk} \partial_j \tilde{\gamma}_{ik}$ with an unconstrained free evolution code as in [20,39–44]. The Einstein equations are solved in Cartesian coordinates. To impose axisymmetric boundary conditions, the Cartoon method [45] is used with the grid size $N \times 3 \times N$ in (x, y, z) which covers a computational domain as $0 \leq x \leq L, 0 \leq z \leq L,$ and $-\Delta \leq y \leq \Delta.$ Here, N and L are constants and $\Delta = L/N.$

The fundamental variables for the hydrodynamics are ρ : rest-mass density, ε : specific internal energy, P : pressure, u^μ : four velocity, and

$$v^i = \frac{dx^i}{dt} = \frac{u^i}{u^t}. \quad (3)$$

As the variables to be evolved in the numerical simulations, we define a weighted density, $\rho_*,$ a weighted four-velocity $\hat{u}_\mu,$ and a specific energy density as

$$\rho_* \equiv \rho w e^{6\phi}, \quad \hat{u}_i = hu_i, \quad \hat{e} \equiv hw - \frac{P}{\rho w}, \quad (4)$$

where $w \equiv \alpha u^t$, and $h \equiv 1 + \varepsilon + P/\rho$. From these variables, the total baryon rest mass and angular momentum of the system, which are conserved quantities in an axisymmetric spacetime, can be defined as

$$M_* = \int d^3x \rho_*, \quad (5)$$

$$J = \int d^3x \rho_* \hat{u}_\varphi. \quad (6)$$

The general relativistic hydrodynamic equations are solved using a so-called high-resolution shock-capturing scheme [46] on the $y = 0$ plane with the cylindrical coordinates (x, z) (in Cartesian coordinates with $y = 0$). Details about our numerical scheme are described in [39].

We neglect effects of viscosity and magnetic fields. The time scale of dissipation and angular momentum transport due to these effects are much longer than the time scale of collapse ~ 100 ms, unless the magnitude of viscosity or magnetic fields is extremely large [47]. Thus neglecting them is an appropriate assumption.

As the slicing condition we impose an ‘‘approximate’’ maximal slicing condition in which $K_k^k \approx 0$ is required [40]. As the spatial gauge, we adopt a dynamical gauge condition [48] in which the equation for the shift vector is written as

$$\partial_t \beta^k = \tilde{\gamma}^{kl}(F_l + \Delta t \partial_t F_l). \quad (7)$$

Here, Δt denotes the time step in numerical computation [21]. Note that in this gauge condition, β^i obeys a hyperbolic-type equation for a sufficiently small value of Δt because the right-hand side of the evolution equation for F_i contains a vector Laplacian term [43]. It has already been illustrated that stable simulations for rotating stellar collapse and merger of binary neutron stars are feasible in this gauge [21,42].

An outgoing-wave boundary condition is imposed for h_{ij} ($\equiv \tilde{\gamma}_{ij} - \delta_{ij}$), \tilde{A}_{ij} , and F_i at the outer boundaries of the computational domain. The condition adopted is the same as that described in [43]. On the other hand, for ϕ and K_k^k , other types of outer boundary conditions are imposed as $r\phi = \text{const}$ and $K_k^k = 0$, respectively.

Existence of a black hole is determined using an apparent horizon finder developed in [49]. We compute the apparent horizon mass M_{AH} which is defined as [50]

$$M_{\text{AH}} = \sqrt{\frac{A}{16\pi}}, \quad (8)$$

where A denotes area of an apparent horizon.

During the numerical simulations, conservation of the Arnowitt-Deser-Misner (ADM) mass, M_{ADM} , and the angular momentum are monitored as code checks. The ADM

mass is defined by

$$M_{\text{ADM}} = \int d^3 \left[\psi^5 (\rho h w^2 - P) + \frac{\psi^5}{16\pi} (\tilde{A}_{ij} \tilde{A}^{ij} - \frac{2}{3} (K_k^k)^2) - \frac{1}{16\pi} \tilde{R} \psi \right], \quad (9)$$

where $\psi \equiv e^\phi$.

For the analysis of numerical results, we define a rest-mass distribution $m_*(j)$ [19], which is the integrated baryon rest mass of fluid elements with the specific angular momentum less than a given value of $j = \hat{u}_\varphi$:

$$m_*(j) \equiv 2\pi \int_{j' < j} \rho_* r^2 dr d(\cos\theta). \quad (10)$$

Similarly, a specific angular momentum distribution is defined according to

$$J(j) \equiv 2\pi \int_{j' < j} \rho_* j' r^2 dr d(\cos\theta). \quad (11)$$

These distribution functions are preserved in axisymmetric spacetimes of ideal fluid. Gauge independence and preservation of these distribution functions in axial symmetry can be proven by the hydrodynamical equations

$$\frac{\partial \rho_*}{\partial t} + \frac{\partial(\rho_* v^I)}{\partial x^I} = 0, \quad (12)$$

$$\frac{\partial(\rho_* j)}{\partial t} + \frac{\partial(\rho_* j v^I)}{\partial x^I} = 0, \quad (13)$$

where the index I denotes the component of ϖ and z .

From these distribution functions, we define a spin parameter distribution as

$$q_*(j) \equiv \frac{J(j)}{m_*(j)^2}. \quad (14)$$

This may be approximately regarded as a spin parameter of the inner region of the core composed of fluid elements with the specific angular momentum less than j .

B. Equations of state

During dynamical evolution, a parametric equation of state is adopted following Müller and his collaborators [29,34,51]. In this equation of state, one assumes that the pressure consists of the sum of polytropic and thermal parts as

$$P = P_{\text{p}} + P_{\text{th}}. \quad (15)$$

P_{p} denotes the cold (zero temperature) nuclear equation of state and is given by $P_{\text{p}} = K_{\text{p}}(\rho) \rho^{\Gamma(\rho)}$ where K_{p} and Γ are functions of ρ . In this paper, we follow [34] for the choice of $K_{\text{p}}(\rho)$ and $\Gamma(\rho)$: For the density smaller than the nuclear density, ρ_{nuc} , we set $\Gamma = \Gamma_1 < 4/3$, and for $\rho \geq \rho_{\text{nuc}}$, $\Gamma = \Gamma_2 > 2$. Namely,

$$P_P = \begin{cases} K_1 \rho^{\Gamma_1}, & \rho \leq \rho_{\text{nuc}}, \\ K_2 \rho^{\Gamma_2}, & \rho \geq \rho_{\text{nuc}}, \end{cases} \quad (16)$$

where K_1 and K_2 are constants. Since P_P should be continuous at $\rho = \rho_{\text{nuc}}$, the relation, $K_2 = K_1 \rho_{\text{nuc}}^{\Gamma_1 - \Gamma_2}$, is required. Following [29,34], the value of K_1 is fixed to be 5×10^{14} cgs. With this choice, the polytropic part of the equation of state for $\rho < \rho_{\text{nuc}}$, in which the degenerate pressure of electrons is dominant, is approximated well. Since the specific internal energy should be also continuous at $\rho = \rho_{\text{nuc}}$, the polytropic part of the specific internal energy, ε_P , is defined as

$$\varepsilon_P = \begin{cases} \frac{K_1}{\Gamma_1 - 1} \rho^{\Gamma_1 - 1}, & \rho \leq \rho_{\text{nuc}}, \\ \frac{K_2}{\Gamma_2 - 1} \rho^{\Gamma_2 - 1} + \frac{(\Gamma_2 - \Gamma_1) K_1 \rho_{\text{nuc}}^{\Gamma_1 - 1}}{(\Gamma_1 - 1)(\Gamma_2 - 1)}, & \rho \geq \rho_{\text{nuc}}. \end{cases} \quad (17)$$

With this setting, a realistic equation of state for high-density, cold nuclear matter is mimicked.

For realistic simulations of stellar core collapse, it would be better to adopt realistic equations of state [52,53]. However, in the realistic equations of state, many microphysical processes are simultaneously taken into account together. In such cases, it is not easy to extract an important element responsible for an output of numerical simulations. With the parametric equations of state, on the other hand, one can systematically investigate dependence of the dynamics of stellar core collapse on the equations of state by changing their own parameters. Therefore, as a first step to the more realistic simulations of rotating stellar core collapse, we adopt the parametric equations of state. We now plan to perform simulations with realistic equations of state. Some discussion comparing the parametric equations of state and a realistic equation of state is presented in Appendix A.

There are four parameters in the parametric equations of state, namely $(\Gamma_1, \Gamma_2, \rho_{\text{nuc}}, \Gamma_{\text{th}})$. In this paper, we choose sets of $(\Gamma_1, \Gamma_2, \rho_{\text{nuc}})$ so that the maximum allowed ADM mass of the cold spherical polytrope becomes an approximately identical value as $M_{\text{ADM,max}} \approx 1.6M_{\odot}$. Note that this value is larger than the mass of neutron stars in binary neutron stars accurately determined, and thus, a reasonable choice [54]. Following [29,34], we typically set $\rho_{\text{nuc}} = 2.0 \times 10^{14} \text{ g/cm}^3$ ($\rho_{14} \equiv \rho_{\text{nuc}} / (10^{14} \text{ g/cm}^3) = 2.0$). For Γ_1 , we choose the three values of 1.32, 1.30, and 1.28. Requiring that the maximum allowed ADM mass should be $\approx 1.6M_{\odot}$, the values of Γ_2 are determined to be 2.25, 2.50, and 2.75, respectively. To investigate the dependence of the output physics on the value of ρ_{nuc} , we also pick up a case with $\rho_{\text{nuc}} = 1.0 \times 10^{14} \text{ g/cm}^3$ ($\rho_{14} = 1.0$) and set $(\Gamma_1, \Gamma_2) = (1.30, 2.22)$ for comparison.

To summarize, the parameter sets adopted in this paper are $(\Gamma_1, \Gamma_2, \rho_{14}) = (1.32, 2.25, 2.0)$, $(1.30, 2.50, 2.0)$, $(1.30, 2.22, 1.0)$, and $(1.28, 2.75, 2.0)$ which are referred to as equations of state ‘‘a,’’ ‘‘b,’’ ‘‘c,’’ and ‘‘d,’’ respectively, (cf. Table I). Although the maximum allowed mass of the cold spherical neutron star in equilibrium is approxi-

TABLE I. Adopted sets of $(\Gamma_1, \Gamma_2, \rho_{\text{nuc}}, \Gamma_{\text{th}})$. The values of Γ_1 , Γ_2 , and ρ_{nuc} are chosen so that the maximum ADM mass of a cold spherical polytrope for each set becomes $\approx 1.6M_{\odot}$.

Model	Γ_1	Γ_2	$\rho_{\text{nuc}} (\text{g/cm}^3)$	Γ_{th}	M_{max}
a	1.32	2.25	2.0×10^{14}	1.32	1.623
b	1.30	2.5	2.0×10^{14}	1.30	1.600
c	1.30	2.22	1.0×10^{14}	1.30	1.599
d	1.28	2.75	2.0×10^{14}	1.28	1.597

mately identical for all of the equations of state, the difference in the values of $(\Gamma_1, \Gamma_2, \rho_{\text{nuc}})$ yields a significant variation in the collapse dynamics and in the criterion for prompt black hole formation.

Figure 1 shows relations between the pressure and the density for each set of $(\Gamma_1, \Gamma_2, \rho_{\text{nuc}})$. It is found that for the smaller value of Γ_1 , the depletion fraction of the pressure for $\rho \leq \rho_{\text{nuc}}$ is increased by a large factor. It is also worthy to note that the equation of state ‘‘c’’ is stiffer than ‘‘b’’ in the density range between 10^{14} and $\approx 2 \times 10^{15} \text{ g/cm}^3$. These result in significant difference in the collapse dynamics and the threshold mass for the prompt black hole formation.

P_{th} is related to the thermal energy density, $\varepsilon_{\text{th}} \equiv \varepsilon - \varepsilon_P$, as

$$P_{\text{th}} = (\Gamma_{\text{th}} - 1)\rho\varepsilon_{\text{th}}. \quad (18)$$

In this paper we set $\Gamma_{\text{th}} = \Gamma_1$ for simplicity. As shown in [36], the collapse dynamics depends rather weakly on Γ_{th} as far as it is in the range $4/3 \approx \Gamma_{\text{th}} \approx 5/3$, besides the fact

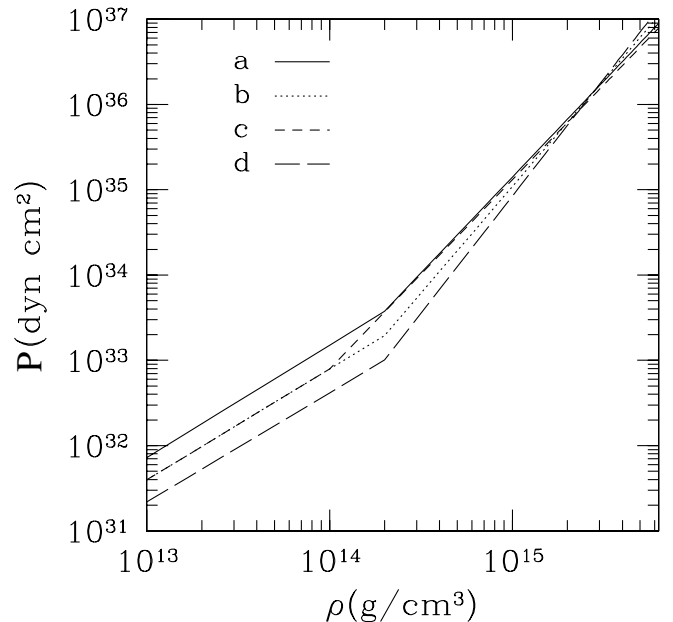


FIG. 1. The pressure, P , as a function of the density, ρ , for cold equations of state with the parameters listed in Table I.

that the oscillation amplitude of a formed protoneutron star depends slightly on it.

To prepare rotating stars in equilibrium as initial conditions, we use the polytropic equations of state with $\Gamma = 4/3$

$$P = K_0 \rho^{4/3} = (K_{\text{deg}} + K_T) \rho^{4/3}, \quad (19)$$

where following [34], K_{deg} is set to be $5 \times 10^{14} \text{ cm}^3/\text{s}^2/\text{gr}^{1/3}$, with which a soft equation of state governed by the electron degenerate pressure is approximated well [13]. Here, K_{deg} and K_1 are related by $K_1 = K_{\text{deg}} \rho_0^{4/3 - \Gamma_1}$ where we set $\rho_0 = 1 \text{ g/cm}^3$. The extra pressure of $P_T \equiv K_T \rho^{4/3}$ denotes the pressure generated by the ideal gas pressure and the radiation pressure that are nonzero only for the finite temperature. The values of K_0 and K_T adopted in the present paper are described in Sec. III. To induce the collapse, we slightly decrease the value of the adiabatic index from $\Gamma = 4/3$ to $\Gamma_1 < 4/3$ at $t = 0$. This implies that at $t = 0$, $P_p = K_{\text{deg}} \rho^{\Gamma_1}$ and $P_{\text{th}} = K_T \rho^{\Gamma_1}$, respectively.

C. Quadrupole formula

In the present work, gravitational waveforms are computed using a quadrupole formula described in [36,55]. In quadrupole formulas, only the +-mode of gravitational waves with $l = 2$ is nonzero in axisymmetric spacetime and it is written as

$$h_+^{\text{quad}} = \frac{\ddot{I}_{zz}(t_{\text{ret}}) - \ddot{I}_{xx}(t_{\text{ret}})}{r} \sin^2 \theta, \quad (20)$$

where I_{ij} denotes a quadrupole moment, \ddot{I}_{ij} its second time derivative, and t_{ret} a retarded time.

In fully general relativistic and dynamical spacetime, there is no unique definition for the quadrupole moment and nor is for \ddot{I}_{ij} . Following a previous paper [55], we choose the simplest definition as

$$I_{ij} = \int \rho_* x^i x^j d^3x. \quad (21)$$

Then, using the continuity equation of the form

$$\partial_t \rho_* + \partial_i (\rho_* v^i) = 0, \quad (22)$$

the first time derivative can be written as

$$\dot{I}_{ij} = \int \rho_* (v^i x^j + x^i v^j) d^3x. \quad (23)$$

To compute \ddot{I}_{ij} , the finite differencing of the numerical result for \dot{I}_{ij} is carried out.

In the following, we present

$$A_2(t_{\text{ret}}) = \ddot{I}_{zz}(t_{\text{ret}}) - \ddot{I}_{xx}(t_{\text{ret}}), \quad (24)$$

in the quadrupole formula. This provides the amplitude of

$l = 2$ mode measured by an observer located in the most optimistic direction (i.e., in the equatorial plane).

The energy power spectrum of gravitational waves is given in [56] as

$$\frac{dE}{df} = \frac{\pi}{2} (4\pi r^2) f^2 \langle |\tilde{h}_+(f)|^2 \rangle \quad (f > 0), \quad (25)$$

where $\tilde{h}_+(f)$ denotes the Fourier transform

$$\tilde{h}_+(f) = \int h_+^{\text{quad}}(t) e^{2\pi i f t} dt, \quad (26)$$

and the bracket denotes the angle-averaged value. This can be expressed in the present case as (e.g. [57])

$$\langle |\tilde{h}_+(f)|^2 \rangle = \frac{8}{15} \frac{1}{r^2} |\tilde{A}_2(f)|^2, \quad (27)$$

where

$$\tilde{A}_2(f) = \int A_2(t) e^{2\pi i f t} dt. \quad (28)$$

Thus, the effective amplitude of gravitational waves observed in the most optimistic direction is denoted by

$$\begin{aligned} h_{\text{eff}} &\equiv \frac{|f A_2(f)|}{r} \\ &= 5.0 \times 10^{-20} \left(\frac{dE/df}{10^{46} \text{ erg/Hz}} \right)^{1/2} \left(\frac{10 \text{ kpc}}{r} \right). \end{aligned} \quad (29)$$

As indicated in [55], it is possible to compute gravitational waves from oscillating and rapidly rotating neutron stars of high values of compactness fairly accurately with the present choice of I_{ij} , besides possible systematic errors for the amplitude of order M/R . For the stellar core collapse in which the outcomes are protoneutron stars of $M/R \sim 0.1-0.2$, it is likely that the wave amplitude is computed within an error of $\sim 10-20\%$. The phase of gravitational waves will be computed very accurately as indicated in [55]. For the stellar core collapse to a black hole, on the other hand, the quadrupole formula will be no longer valid because the value of M/R is high and, moreover, quasinormal mode ringing of the formed black hole is not taken into account.

III. INITIAL CONDITIONS AND COMPUTATIONAL SETTING

A. Initial conditions

Recent numerical study [58,59] for stellar evolution of very massive and low metallicity stars from main-sequence to the pre-iron-core-collapse suggests that initially massive stars evolve to form an iron core of mass $\geq 2M_{\odot} - 3M_{\odot}$. Taking these fact into account, we consider a wide range of the mass for the progenitor of the collapse as $2M_{\odot} \leq M \leq 3M_{\odot}$.

It should be addressed that such large mass of the iron core may not be a special product of low metallicity or

large progenitor mass. Recently, Hirschi *et al.* [60] study presupernova evolution of *rotating* massive star of solar metallicity and show that mass of the iron core at the onset of the collapse depends strongly on the treatment of both convection and rotation. They find that the rotation significantly increases (by a factor of ~ 1.5) the core mass: An iron core of mass of $\approx 2.0M_\odot$ is formed from the ZAMS (zero-age main sequence) of $15M_\odot$ by including the rotation while its nonrotating counterpart yields an iron core of mass $\approx 1.5M_\odot$. This result is quite different from that in [61]. This suggests that mass of the iron core at the onset of collapse may depend sensitively on the chemical abundance, and the stellar rotation as well as the magnitude of the viscosity and the mixing length which are not well understood.

The central density and the central temperature of such very massive iron cores are $\rho_c \gtrsim 5 \times 10^9 \text{ g/cm}^3$ and $T_c \sim 10^{10} \text{ K}$, respectively [59]. Thus, we set the central density of the initial conditions to be 10^{10} g/cm^3 . The electrons under such a high density are extremely degenerate even with $T \approx 10^{10} \text{ K}$, since ratio of the Fermi energy of free electrons, ε_F , to thermal energy, $k_B T$, is much larger than unity [13] according to

$$\frac{\varepsilon_F}{k_B T} \approx 10 \left(\frac{Y_e}{0.45} \right)^{1/3} \left(\frac{\rho}{10^{10} \text{ g/cm}^3} \right)^{1/3} \left(\frac{T}{10^{10} \text{ K}} \right)^{-1}. \quad (30)$$

Therefore, the main contribution of the pressure comes from the electron degenerate pressure that is denoted by the polytropic form as $P_{\text{deg}} = K_{\text{deg}} \rho^{4/3}$.

In addition to the electron degenerate pressure, the thermal and radiation pressure should be taken into account. The adiabatic index relevant for them in the iron core may be close to $4/3$ at the onset of the collapse since the photo-dissociation of the irons are accelerated with increasing the density to reduce the pressure. Hence, we put the gas and radiation pressure together into the polytropic form as

$$P_T \equiv P_{\text{gas}} + P_{\text{rad}} = K_T \rho^{4/3}. \quad (31)$$

With these assumptions, rotating polytropes in equilibrium with the polytropic index $\Gamma = 4/3$ and the polytropic constant $K_0 = K_{\text{deg}} + K_T$ [see Eq. (19)] are given as the initial models of rotating iron cores.

The iron core model adopted in this paper is nothing more than a simplified one. The nature is more complicated and the iron core of the evolved massive star are not simple polytropes [33]. We will nevertheless use the term ‘‘iron core’’ in the following, to emphasizing that we aim at clarifying the threshold mass of the *iron core* for the prompt black hole formation.

We adopt the values of $K_{14} \equiv K_0/10^{14}$ (cgs) to be 6.0, 6.5, 6.75, 7.0, 7.25, 7.5, 7.75, and 8.0, which we refer to models A, B, C, D, E, F, G, and H, respectively, (cf. Table II). In the Newtonian case, mass of the $\Gamma = 4/3$ spherical polytrope is given by $M \approx 4.555(K_0/G)^{3/2}$.

Thus, for the adopted values of K_0 , the ADM mass of the initial spherical iron cores are $M_{\text{ADM}}/M_\odot \approx 2.0, 2.2, 2.3, 2.4, 2.6, 2.7, 2.9,$ and 3.0 , respectively, (see Table II). These values are larger than the maximum allowed ADM mass, $\approx 1.6M_\odot$, of the spherical cold polytrope adopted in this paper. Namely, in the absence of shock heating and rotation, the core collapses to a black hole.

For our choice of the iron core mass, the corresponding helium core mass is $M_{\text{He}}/M_\odot \approx 17, 22, 25, 30, 32, 35, 40,$ and 42 for models A, B, C, D, E, F, G, and H, respectively, according to the calculation by Umeda and Nomoto [59]. Note that these values are larger than a critical value of helium core mass for direct black hole formation $\approx 15M_\odot$ estimated in [62,63].

The velocity profiles of equilibrium rotating cores are given according to a popular relation [64,65]

$$u^t u_\phi = \varpi_d^2 (\Omega_a - \Omega), \quad (32)$$

where Ω_a denotes the angular velocity along the rotational axis, and ϖ_d is a constant. In the Newtonian limit, the rotational profile is written as

$$\Omega = \Omega_a \frac{\varpi_d^2}{\varpi^2 + \varpi_d^2}. \quad (33)$$

Thus, ϖ_d controls the steepness of differential rotation. In this paper, we pick up mainly the rigidly rotating models in which $\varpi_d \rightarrow \infty$. For illustration of the effect of differential rotation, we select differentially rotating models with $A \equiv \varpi_d/R_e = 1$ and 0.5 (see Table III).

For rigidly rotating initial models, we choose the axial ratio R_p/R_e of polar radius, R_p , to equatorial radius, R_e , as 1 (spherical configuration), 119/120, 115/120, 110/120, 105/120, 100/120, 90/120, and 80/120. The models with these axial ratios are referred to as models X0, X1, X15, X2, X25, X3, X4, and X5, where X denotes A–H. For example, a model with $K_{14} = 7.0$ and $R_p/R_e = 80/120$ is abbreviated as D5. Note that for models with $R_p/R_e = 80/120$, the angular velocity at the equatorial stellar surface is nearly equal to the Keplerian velocity, namely, a rapidly rotating initial condition near the mass-shedding limit is chosen for this case. On the other hand, differentially rotating initial models are chosen only for a selected set of parameters with $K_{14} = 7.0$ and 8.0 , since the purpose in this paper is to clarify the effect of differential rotation, comparing the results with those for the rigidly rotating initial models of nearly identical values of mass and angular momentum.

In Tables II and III, several fundamental quantities for the models adopted in the present numerical computation are listed. Here, q is a nondimensional spin parameter defined by $J/M_{\text{ADM}}^2 T_{\text{tot}}$ and W are the rotational kinetic energy and the gravitational potential energy, and defined according to [66,67]

TABLE II. The values of K_0 , axial ratio R_p/R_e , ADM mass M_{ADM} , equatorial circumferential radius R_{cc} , ratio of the rotational kinetic energy, T_{rot} , to the gravitational potential energy, W , nondimensional spin parameter $q \equiv J/M_{\text{ADM}}^2$, and angular velocity Ω_a for rigidly rotating iron cores in equilibrium used as the initial condition for numerical simulation.

Model	K_0 (cgs)	R_p/R_e	$M_{\text{ADM}}(M_\odot)$	R_{cc} (km)	T_{rot}/W	q	Ω_a (1/s)
A0	6.0×10^{14}	1	1.920	1717	0.0	0.0	0.0
A1	6.0×10^{14}	119/120	1.921	1718	3.98×10^{-4}	0.234	0.904
A2	6.0×10^{14}	110/120	1.940	1836	3.68×10^{-3}	0.716	2.71
A3	6.0×10^{14}	100/120	1.957	1999	6.51×10^{-3}	0.959	3.56
A4	6.0×10^{14}	90/120	1.967	2207	8.28×10^{-3}	1.086	3.98
A5	6.0×10^{14}	80/120	1.971	2478	8.88×10^{-3}	1.128	4.11
B0	6.5×10^{14}	1	2.163	1793	0.0	0.0	0.0
B1	6.5×10^{14}	119/120	2.163	1793	3.98×10^{-4}	0.224	1.01
B2	6.5×10^{14}	110/120	2.185	1914	3.67×10^{-3}	0.688	2.71
B3	6.5×10^{14}	100/120	2.203	2080	6.50×10^{-3}	0.921	3.56
B4	6.5×10^{14}	90/120	2.215	2300	8.27×10^{-3}	1.044	3.98
B5	6.5×10^{14}	80/120	2.219	2582	8.87×10^{-3}	1.084	4.11
C0	6.75×10^{14}	1	2.286	1812	0.0	0.0	0.0
C1	6.75×10^{14}	119/120	2.289	1824	3.97×10^{-4}	0.221	0.901
C15	6.75×10^{14}	115/120	2.298	1876	1.92×10^{-3}	0.487	1.97
C2	6.75×10^{14}	110/120	2.310	1948	3.67×10^{-3}	0.675	2.70
C25	6.75×10^{14}	105/120	2.321	2030	5.20×10^{-3}	0.807	3.20
D0	7.0×10^{14}	1	2.412	1845	0.0	0.0	0.0
D1	7.0×10^{14}	119/120	2.414	1859	3.97×10^{-4}	0.217	0.902
D15	7.0×10^{14}	115/120	2.425	1909	1.92×10^{-3}	0.478	1.97
D2	7.0×10^{14}	110/120	2.438	1986	3.67×10^{-3}	0.663	2.70
D25	7.0×10^{14}	105/120	2.449	2065	5.20×10^{-3}	0.792	3.20
D3	7.0×10^{14}	100/120	2.459	2162	6.49×10^{-3}	0.888	3.55
D4	7.0×10^{14}	90/120	2.472	2387	8.26×10^{-3}	1.006	3.97
D5	7.0×10^{14}	80/120	2.476	2679	8.86×10^{-3}	1.045	4.10
E2	7.25×10^{14}	110/120	2.568	2019	3.66×10^{-3}	0.652	2.70
E25	7.25×10^{14}	105/120	2.580	2103	5.20×10^{-3}	0.780	3.19
E3	7.25×10^{14}	100/120	2.590	2198	6.49×10^{-3}	0.873	3.55
E4	7.25×10^{14}	90/120	2.604	2428	8.25×10^{-3}	0.989	3.97
E5	7.25×10^{14}	80/120	2.608	2726	8.86×10^{-3}	1.03	4.09
F0	7.5×10^{14}	1	2.672	1909	0.0	0.0	0.0
F1	7.5×10^{14}	117/120	2.680	1951	1.17×10^{-3}	0.361	1.55
F2	7.5×10^{14}	110/120	2.700	2056	3.66×10^{-3}	0.641	2.71
F3	7.5×10^{14}	100/120	2.723	2238	6.49×10^{-3}	0.858	3.55
F4	7.5×10^{14}	90/120	2.738	2471	8.26×10^{-3}	0.972	3.97
F5	7.5×10^{14}	80/120	2.742	2773	8.86×10^{-3}	1.010	4.10
G0	7.75×10^{14}	90/120	2.874	2510	8.24×10^{-3}	0.957	3.96
G5	7.75×10^{14}	80/120	2.879	2818	8.85×10^{-3}	0.993	4.09
H0	8.0×10^{14}	1	2.940	1972	0.0	0.0	0.0
H5	8.0×10^{14}	80/120	3.016	2864	8.84×10^{-3}	0.978	4.10

$$T_{\text{rot}} \equiv \frac{1}{2} \int d^3x \rho_* \hat{u}_\varphi \Omega, \quad (34)$$

$$W \equiv M_* + \int \rho_* \varepsilon d^3x - M_{\text{ADM}} + T_{\text{rot}}, \quad (35)$$

where W is defined to be positive. Note that for the rigidly rotating case, the maximum value of T_{rot}/W is ≈ 0.009 .

For the rigidly or weakly differentially rotating stars, the stability against nonaxisymmetric perturbation is determined by T_{rot}/W [68]. A star with $T_{\text{rot}}/W \geq 0.27$ and $T_{\text{rot}}/W \geq 0.14$ will become unstable against the nonaxisymmetric dynamical and secular instabilities, respectively. Here, the secular timescale is much longer than the collapse timescale, so that the dynamical instabilities are only relevant during collapse and bounces. Since we

TABLE III. The values of K_0 , $A \equiv \varpi_a/R_e$, M_{ADM} , R_e , T_{rot}/W , $q \equiv J/M_{\text{ADM}}^2$, and angular velocity at the rotational axis Ω_a for differentially rotating initial models.

Model	K_0 (cgs)	A	$M_{\text{ADM}}(M_\odot)$	R_e (km)	T_{rot}/W	q	Ω_a (1/s)
D20d1	7.0×10^{14}	1.0	2.437	1912	3.54×10^{-3}	0.647	3.06
D22d1	7.0×10^{14}	1.0	2.441	1924	4.12×10^{-3}	0.698	3.29
D23d1	7.0×10^{14}	1.0	2.445	1936	4.69×10^{-3}	0.746	3.50
D25d1	7.0×10^{14}	1.0	2.450	1950	5.26×10^{-3}	0.791	3.69
D15d05	7.0×10^{14}	0.5	2.424	1858	1.75×10^{-3}	0.440	2.84
D17d05	7.0×10^{14}	0.5	2.430	1866	2.63×10^{-3}	0.541	2.84
D20d05	7.0×10^{14}	0.5	2.437	1874	3.52×10^{-3}	0.626	3.47
D25d05	7.0×10^{14}	0.5	2.444	1881	4.42×10^{-3}	0.702	4.21
H5d1	8.0×10^{14}	1.0	3.019	2190	9.03×10^{-3}	0.978	4.75
H5d05	8.0×10^{14}	0.5	3.020	2054	8.98×10^{-3}	0.941	6.31

assume that the rotating iron core collapse proceeds in an axisymmetric manner, it is important to ensure that the iron core should not spin up to be dynamically unstable against nonaxisymmetric deformation. We will discuss the spin-up and the stabilities of the inner cores formed after the bounce in Sec. IV D 2.

For the differentially rotating case with a small value of A , it is possible to make equilibrium states with $T_{\text{rot}}/W \gg 0.009$. With such an initial condition, the collapsing core may form a differentially rotating object of a highly non-spherical shape and of a high value of T_{rot}/W [38,30]. It is also known that rapidly rotating neutron stars of a high degree of differential rotation is dynamically unstable against nonaxisymmetric deformation even for $T_{\text{rot}}/W = O(0.01)$ (e.g., [69] and references therein). To follow such collapse, a nonaxisymmetric simulation will be necessary. In this paper, we do not choose such initial conditions and focus only on dynamically stable cases against nonaxisymmetric deformation. The collapse of highly differentially rotating initial conditions is studied in three-dimensional simulations in [38].

B. Computational settings

The central density increases from 10^{10} g/cm³ to $\geq 10^{15}$ g/cm³ during the collapse. This implies that the characteristic length scale of the system varies by a factor of ~ 100 . To compute such a collapse accurately saving the CPU time efficiently, a regridding technique as described in [19,36] is helpful. The regridding is carried out whenever the characteristic radius of the collapsing star decreases by a factor of a few. At each regridding, the grid spacing is decreased by a factor of 2. All the quantities in the new grid are calculated using the cubic interpolation. To avoid discarding the matter in the outer region, we also increase the grid number at the regridding.

For the regridding, we define a relativistic gravitational potential $\Phi_c \equiv 1 - \alpha_c$ ($\Phi_c > 0$). Since Φ_c is approximately proportional to M/R , Φ_c^{-1} can be used as a measure of the characteristic length scale of the core for the regridding. We typically choose N at each regridding in the

following manner. From $t = 0$ to the time at which $\Phi_c = 0.025$, we set $N = 620$ with the grid spacing $\Delta R_e/600$. At $\Phi_c = 0.025$, the characteristic stellar radius becomes approximately one fourth of the initial value. Then, the first regridding is performed; the grid spacing is changed to the half of the previous one and the grid number is increased to $N = 1020$. Subsequently, the value of N is chosen in the following manner; for $0.025 \leq \Phi_c \leq 0.05$, we set $N = 1020$; for $0.05 \leq \Phi_c \leq 0.1$, we set $N = 1700$; and for $0.1 \leq \Phi_c \leq 0.25$, we set $N = 2500$, and keep this number until the termination of the simulations. For the typical cases, the physical size of the grid spacing is $\Delta \sim 4$ km at the beginning of simulations and ~ 0.5 km at the end.

In the case of black hole formation, Φ_c approaches to 1. In this case, we carry out one more regridding at the time of $\Phi_c = 0.25$. In this final regridding, the grid spacing is made half while keeping $N = 2500$. For the typical cases in which a black hole is formed, the physical size of the grid spacing is $\Delta \sim 4$ km at the beginning of simulations and ~ 0.25 km at the end. In this treatment, the total discarded fraction of the baryon rest-mass which is located outside the new regridded domains is $\leq 4\%$.

Simulations for each model with the higher grid resolution are performed for 40 000–100 000 time steps. The required CPU time for one model is about 30–90 hours using 8 processors of FACOM VPP 5000 at the data processing center of National Astronomical Observatory of Japan.

IV. NUMERICAL RESULTS

A. General feature of the collapse

We first summarize the outline of the dynamics of stellar core collapse. Detailed features of the collapse will be presented in the subsequent subsections. In Figs. 2–5, we display evolution of the central density ρ_c and the central value of the lapse function α_c for selected models. As indicated in these figures, rotating stellar core collapse to a neutron star can be divided into three phases; the infall phase, the bounce phase, and the ring-down (or post-bounce oscillation) phase [26,29].

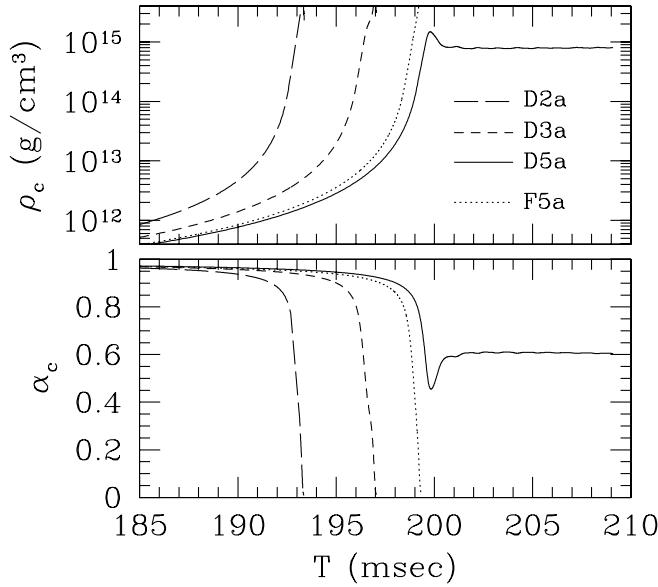


FIG. 2. Evolution of the central density ρ_c (upper panel) and the central value of the lapse function α_c (lower panel) for models D2a (long dashed curve), D3a (dashed curve), D5a (solid curve), and F5a (dotted curve).

The infall phase sets in due to the onset of the gravitational instability of the progenitor triggered by the sudden softening of the equation of state which is associated with the reduction of the adiabatic index. During this phase, the central density, ρ_c , (the central value of the lapse function, α_c), monotonically increases (decreases) until it reaches the nuclear density, provided that the core is not very rapidly rotating initially. The inner part of the core, which

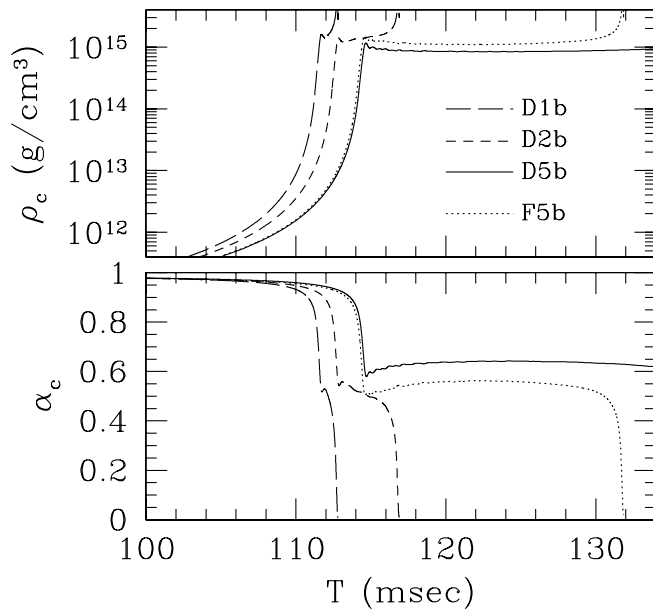


FIG. 3. The same as Fig. 2 but for models D1b (long dashed curve), D2b (dashed curve), D5b (solid curve), and F5b (dotted curve).

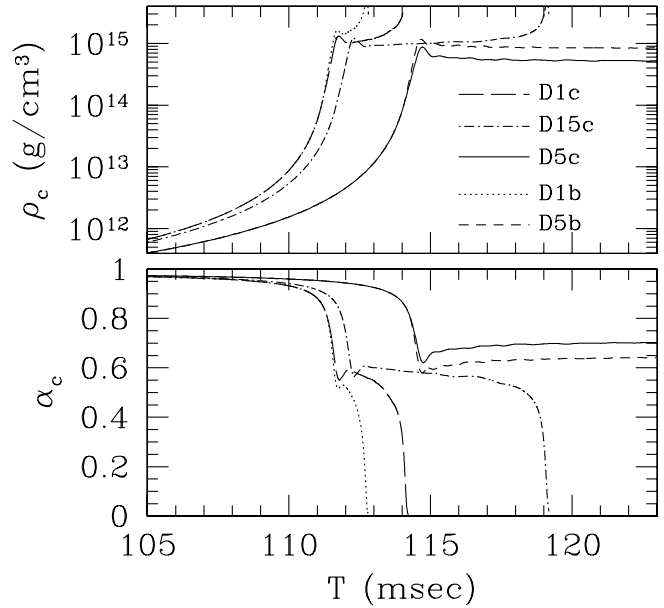


FIG. 4. The same as Fig. 2 but for models D1c (long dashed curve), D15c (dotted dashed curve), D5c (solid curve). Results for models D1b (dotted curve) and D5b (dashed curve) are also displayed for comparison.

collapses nearly homologously with a subsonic infall velocity, constitutes the inner core. On the other hand, the outer region in which the infall velocity is supersonic constitutes the outer core [26,29].

The bounce phase sets in when the density around the central region exceeds the nuclear density. At this phase,

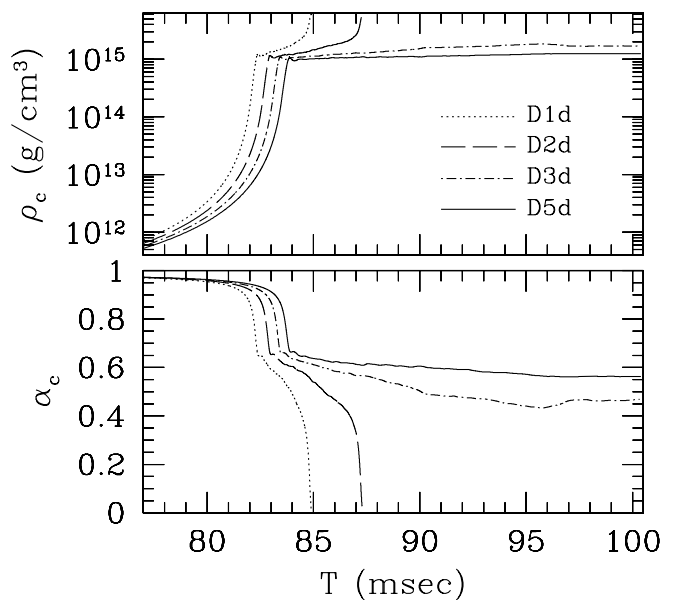


FIG. 5. The same as Fig. 2 but for models D1d (dotted curve), D2d (long dashed curve), D3d (dotted dashed curve), and D5d (solid curve).

TABLE IV. Summary of the outcome in the iron core collapse with rigidly rotating initial models. The adopted equations of state are discriminated by a single alphabet: "a" for $(\Gamma_1, \Gamma_2, \rho_{14}) = (1.32, 2.25, 2.0)$, "b" for $(1.3, 2.50, 2.0)$, c for $(1.3, 2.22, 1.0)$, and d for $(1.28, 2.75, 2.0)$. "BH" implies that a black hole (BH) is formed in a dynamical time scale of the collapse. "no BH" implies that a black hole is not formed promptly. "... " in the last column implies that we did not perform simulations for such models.

Initial model	K_0 (cgs)	R_p/R_e	$M_{\text{ADM}}(M_\odot)$	q	Adopted equations of state			
					a	b	c	d
B0	6.5×10^{14}	1	2.163	0.0	BH	BH	no BH	BH
B1	6.5×10^{14}	119/120	2.163	0.217	no BH	no BH	no BH	no BH
B2	6.5×10^{14}	110/120	2.185	0.688	no BH	no BH	no BH	no BH
B3	6.5×10^{14}	100/120	2.203	0.921	no BH	no BH	no BH	no BH
B4	6.5×10^{14}	90/120	2.215	1.044	no BH	no BH	no BH	no BH
B5	6.5×10^{14}	80/120	2.219	1.084	no BH	no BH	no BH	no BH
C0	6.75×10^{14}	1	2.286	0.0	BH	BH	BH	...
C1	6.75×10^{14}	119/120	2.289	0.221	BH	BH	no BH	...
C15	6.75×10^{14}	115/120	2.298	0.487	BH	BH	no BH	...
C2	6.75×10^{14}	110/120	2.310	0.675	BH	no BH	no BH	...
C25	6.75×10^{14}	105/120	2.321	0.807	no BH	no BH	no BH	...
D0	7.0×10^{14}	1	2.412	0.0	BH	BH	BH	BH
D1	7.0×10^{14}	119/120	2.414	0.217	BH	BH	BH	BH
D15	7.0×10^{14}	115/120	2.425	0.478	BH	BH	BH	BH
D2	7.0×10^{14}	110/120	2.438	0.663	BH	BH	no BH	BH
D25	7.0×10^{14}	105/120	2.449	0.792	BH	BH	no BH	BH
D3	7.0×10^{14}	100/120	2.459	0.888	BH	no BH	no BH	no BH
D4	7.0×10^{14}	90/120	2.472	1.006	no BH	no BH	no BH	no BH
D5	7.0×10^{14}	80/120	2.476	1.045	no BH	no BH	no BH	no BH
E2	7.25×10^{14}	110/120	2.568	0.652	BH	BH	BH	...
E25	7.25×10^{14}	105/120	2.580	0.780	BH	BH	no BH	...
E3	7.25×10^{14}	100/120	2.590	0.873	BH	BH	no BH	...
E4	7.25×10^{14}	90/120	2.604	0.989	BH	no BH	no BH	...
E5	7.25×10^{14}	80/120	2.608	1.03	BH	no BH	no BH	...
F0	7.5×10^{14}	1	2.672	0.0	BH	BH	BH	BH
F1	7.5×10^{14}	119/120	2.680	0.361	BH	BH	BH	BH
F2	7.5×10^{14}	110/120	2.700	0.641	BH	BH	BH	BH
F3	7.5×10^{14}	100/120	2.723	0.858	BH	BH	BH	BH
F4	7.5×10^{14}	90/120	2.738	0.972	BH	BH	no BH	BH
F5	7.5×10^{14}	80/120	2.742	1.010	BH	BH	no BH	BH
G4	7.75×10^{14}	90/120	2.874	0.957	BH	BH	BH	...
G5	7.75×10^{14}	80/120	2.879	0.993	BH	BH	BH	...
H0	8.0×10^{14}	1	2.940	0.0	BH	BH	BH	BH
H5	8.0×10^{14}	80/120	3.016	0.978	BH	BH	BH	BH

the inner core decelerates rapidly due to (a) the sudden stiffening of the equation of state or (b) the strong centrifugal force. Hereafter, we pay attention to the case (a) since the collapse is halted due to the sudden stiffening of the equation of state for all the models (cf. Figures 2–5). Because of its large inertia and large kinetic energy induced by the infall, the inner core overshoots its hypothetical equilibrium state. The degree of the overshooting depends on the mass, the amount of rotational kinetic energy, and the stiffness of the equation of state.

If its mass is not too large, the inner core experiences a bounce. The stored internal energy of the inner core at maximum compression is released through a strong pres-

sure wave generated inside the inner core [26]. The pressure wave travels from the center to the outer region until it reaches the sonic point located at the edge of the inner core. Since the sound cones tilt inward beyond the sonic point, the pressure disturbance cannot travel further and forms a shock just inside the sonic point. During the formation of the shock, the inner core transfers its kinetic energy to the shock through compressional work that powers the shock [26,70]. It is important to note that the shock is formed at the outer edge of the inner core, and hence, the bulk of the inner core matter never undergoes shock heating and acceleration. Therefore, the shock heating is relatively less efficient for models with larger mass of the inner core.

On the other hand, if the mass and inertia of the inner core at the bounce are sufficiently large, the pressure supplied by the sudden stiffening of the equation of state and the centrifugal force cannot halt the collapse. Then, the inner core will promptly collapse to a black hole without any distinct bounce (cf. models D2a, D3a, and D5a in Fig. 2 in which a black hole is formed). As illustrated in Sec. IV B 2, shocks do not propagate outward in such cases.

In the ring-down phase, the inner core oscillates quasiradially and then settles down to a quasistationary state, since the compressional work done by the inner core on the matter of the outer region leads to damping of the oscillation. In this phase, the amplitude of the oscillation and the strength of shocks generated by the outward oscillation depend on the stiffness of the equation of state for the formed protoneutron star. In the outer region, on the other hand, shock waves propagate and are accelerated due to the density gradient in the outer core. They sweep materials of the outer envelopes, and convert the infall kinetic energy into the thermal energy, which helps further driving the shock outward. However, if the explosion is too weak to eject sufficient matter of the progenitor star, the subsequent fallback of the matter into the formed protoneutron star will trigger formation of black hole.

B. Criterion for prompt black hole formation

In Table IV, we summarize the outcomes in the iron core collapse for all of rigidly rotating initial models listed in Table II and with equations of state listed in Table I. It is important to note that even for models in which a black hole is not formed promptly (models “no BH”), a long-term fallback of matter may lead to black hole formation. In this paper, we do not study such long-term black hole formation. Since the simulations are performed for the iron core (only part of the whole star), we stop the simulations when the shock front reaches its surface located at a radius of ~ 1000 km. To follow the collapse due to the fallback, it would be necessary to take into account not only the iron core but the carbon-oxygen envelope. Also, neutrino cooling that is ignored in this paper will play a role for a long-term fallback with the duration > 100 ms [71].

Figure 6 illustrates that the threshold mass for the prompt black hole formation depends on the adopted equation of state as well as the angular momentum. In the following section, we describe, in more detail, the dependence of the threshold mass on thermal pressure, rotation, differential rotation, and adopted equations of state, separately.

1. Contribution of thermal pressure

First, we focus on spherical collapse. Because of no rotational effect in this case, the threshold mass depends only on equations of state. Figure 6 shows that the threshold mass for the prompt black hole formation locates

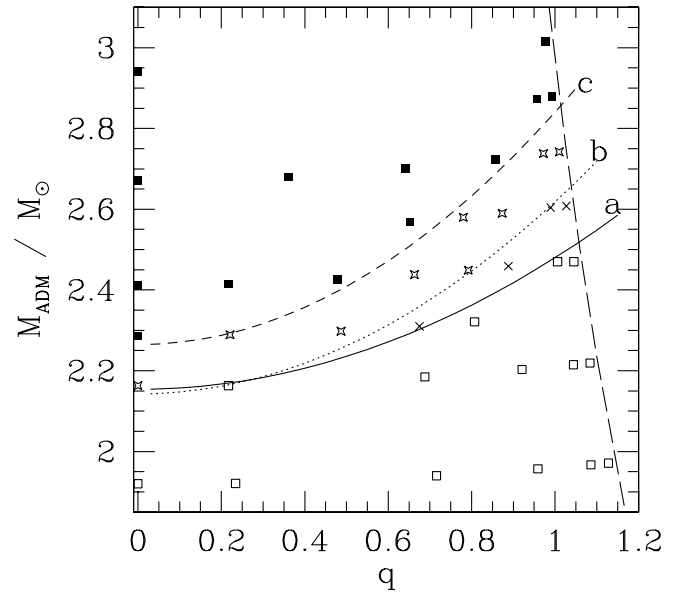


FIG. 6. The distribution map of the outcome in the iron core collapse for rigidly rotating initial models. The horizontal and vertical axes denote the spin parameter q and M_{ADM} . The filled squares denote the models whose final outcome is a black hole irrespective of the equations of state. The open stars denote the models whose final outcome is a black hole for the equations of state of a and “b,” and a neutron star for the equation of state “c.” The crosses denote the models whose final outcome is a black hole only for the equations of state “a.” The open squares indicate no black hole formation irrespective of the equations of state. The solid, dotted, and dashed curves indicate the threshold mass above which a black hole is formed as a result of the collapse for the equations of state “a,” “b,” and “c,” respectively, (see Sec. IV B 4 for locating these curves). The long dashed curve denotes the mass-shedding limit for rigidly rotating initial models; i.e., no equilibrium configurations for rigidly rotating initial condition exist in the right-hand side of this curve.

between $\approx 2.1M_{\odot}$ (model A0) and $\approx 2.3M_{\odot}$ (model C0) depending on the adopted equations of state. This value is by 20–40% larger than the maximum allowed mass for the cold spherical polytrope $\approx 1.6M_{\odot}$.

For the equations of state “a” and “b,” the threshold mass is ≈ 2.1 – $2.2M_{\odot}$. On the other hand, for the equation of state c in which the value of Γ_1 is the same as the equation of state b but the value of ρ_{nuc} is smaller, the threshold mass is $\approx 2.3M_{\odot}$. This fact suggests that magnitude of the thermal pressure P_{th} generated by the shocks is larger for the equations of state with the smaller value of ρ_{nuc} . This difference in the strength of the shock results from the difference in the collapse dynamics. Detailed discussions about the dynamics of the collapse are presented in the next subsection.

2. Dependence on Γ_1 and Γ_2

As discussed and illustrated in [29,34,36], the most important parameter for the dynamics of the collapse dur-

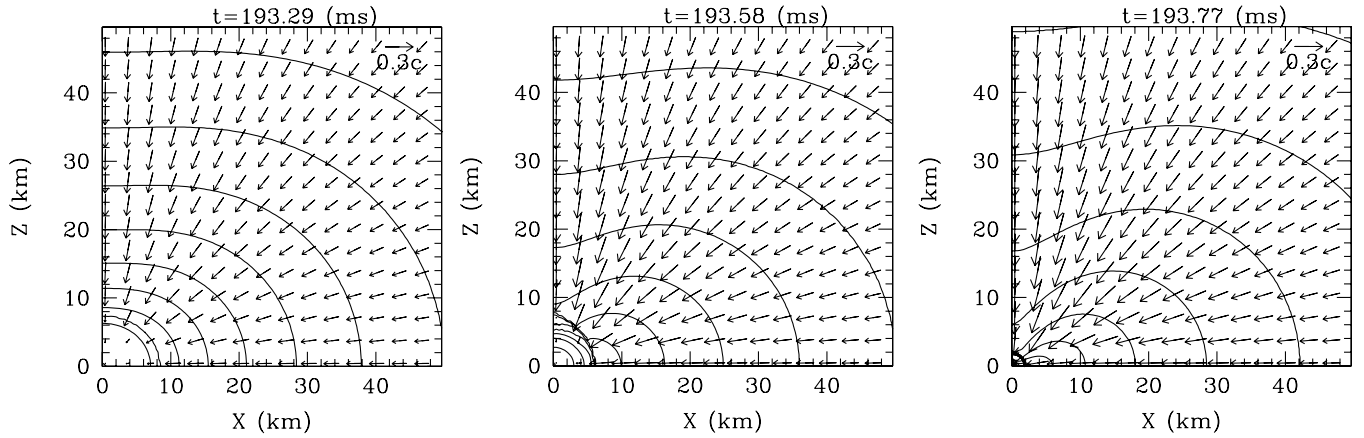


FIG. 7. Snapshots of the density contour curves and velocity vectors in the x - z plane for model D2 with the equation of state “a,” at $t = 193.29, 193.58,$ and 193.77 ms. The density contour curves are drawn for $\rho/\rho_{\max} = 10^{-0.4j}$, ($j = 0, 1, 2, \dots, 20$) where ρ_{\max} is the maximum density at the selected time slices. The thick solid curve in the last panel denotes the location of the apparent horizon.

ing the infall phase is Γ_1 . For the smaller value of Γ_1 (for the larger value of $|\Gamma_1 - 4/3|$), the depleted pressure at $t = 0$ is larger. As a result, the collapse is accelerated more and the elapsed time in the infall phase is shorter. Furthermore, since the depleted fraction of the pressure is larger in the central region than in the outer region for the smaller value of Γ_1 , the collapse in the central region proceeds more rapidly. Accordingly, the iron core contracts less coherently and only the collapse in the inner region of the iron core is accelerated. Therefore, the mass of the inner core at the bounce phase is smaller for the smaller value of Γ_1 . The smaller mass of inner core indicates that the fraction of the iron core which undergoes the shock heating is larger since the shock wave is generated at the outer edge of the inner core. Therefore, the contribution of the thermal pressure to the inner core is more important for models with the smaller value of Γ_1 .

Since the mass of the inner core in the infall and bounce phases is larger for the larger value of Γ_1 , the degree of the

overshooting of the inner core at the bounce phase is larger, due to the stronger gravitational attraction force. Also, for the smaller value of Γ_2 , the degree of the overshooting at the bounce phase is larger since a relatively higher density is required to supply the sufficient pressure to halt the collapse. In the case that mass of the inner core is not so large as to collapse to a black hole, the larger overshooting results in stronger shock generation, since the stored energy of the inner core at the bounce becomes larger (cf. Sec. IV D 1). However, the larger overshooting also increases the risk of collapsing to a black hole since the compactness (the value of α_c) at the bounce becomes larger (smaller).

To understand the dependence of the collapse on equations of state in more details, we generate Figs. 7 and 8, in which we display the snapshots of the density contour curves and velocity vectors in the x - z plane for models D2a and D2b. For models with the equation of state a in which $\Gamma_1 = 1.32$ and $\Gamma_2 = 2.25$, the collapse proceeds

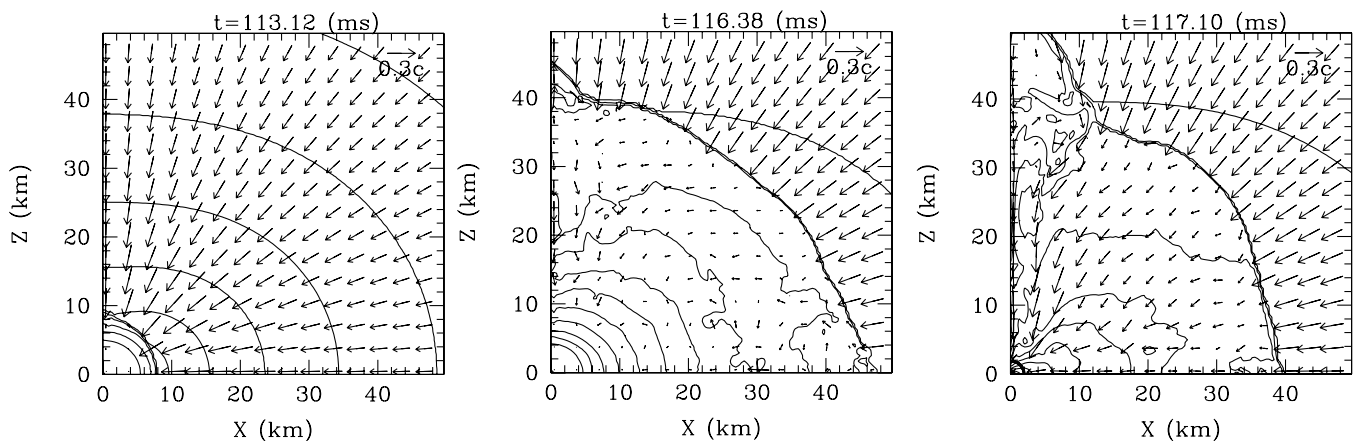


FIG. 8. The same as Fig. 7 but for model D2 with the equation of state “b” at $t = 113.12, 116.38,$ and 117.10 ms. The thick solid curve in the last panel denotes the location of the apparent horizon.

coherently due to the fact that Γ_1 is close to $4/3$, and hence, the mass of the inner core increases to be larger than the maximum allowed mass of the corresponding rotating neutron star at the bounce. Consequently, the inner core promptly collapses to a black hole without generating shocks (cf. Figure 7). This result indicates that for the smaller value of $|\Gamma_1 - 4/3|$, the prompt black hole formation is more liable and the threshold mass of the iron core for the prompt black hole formation is smaller.

For the equations of state “b” and “d,” on the other hand, the collapse proceeds less coherently due to the smaller values of Γ_1 (the larger values of $|\Gamma_1 - 4/3|$). As a result, the mass of the inner core at the bounce is below the maximum allowed mass, and hence, the inner core experiences a bounce and forms a compact protoneutron star for a while before collapsing to a black hole. Also, the shock is formed at the outer edge of the inner core and then propagates outward (cf. Figure 8). This implies that the thermal pressure which helps supporting the inner core is generated in contrast to the case for model D2a. Because of this difference, the threshold mass of the iron core for the prompt black hole formation with the equation of state b is larger than that for “a.” However, the shock formed is not strong enough to blow up the sufficient matter outward even for model D2b: A part of the matter in the outer region falls into the inner core located at the center. This fallback leads to an accretion induced collapse to a black hole (see the third panel Fig. 8).

On the other hand, we do not find significant difference in the threshold mass for the prompt black hole formation between the equations of state “b” and “d” (see Table IV). The plausible reason is described as follows. First, since the mass of the inner core formed at the bounce is smaller for models with the equation of state “d,” the larger fraction of the matter inside the *protoneutron star* will experience the shock heating. On the other hand, the shock wave itself is weaker for the equation of state d since the amplitude of the core bounce and the value of $\Gamma_{\text{th}} (= \Gamma_1)$ is smaller. These two contrary effects cancel each other resulting in approximately the same threshold mass for the prompt black hole formation. A more sophisticated parameter study is required to clarify the small difference in the threshold mass.

3. Dependence on ρ_{nuc}

In Fig. 4, we show the evolution of ρ_c and α_c for models D1c and D15c, for which a black hole is formed promptly as a result of the collapse. For comparison, the result for model D1b is shown together. The evolution of ρ_c and α_c with two equations of state “b” and “c” are identical during the infall phase. However, in the bounce and subsequent phases, increase of ρ_c (decrease of α_c) is delayed and the value of ρ_c (α_c) is smaller (larger) for the equation of state “c.” This is a result from the fact that the sudden

stiffening occurs at an earlier stage of the collapse with the equation of state c due to the smaller value of ρ_{nuc} .

Figure 4 also indicates that the amplitude of oscillation of the inner core at the bounce is larger for models with the equation of state “c.” Several effects are responsible for this result. First, the small value of ρ_{nuc} in the equation of state c results in a smaller mass of the inner core and smaller averaged density at the bounce. As mentioned in Sec. IV B 2, the smaller mass of the inner core results in the fact that a larger amount of the matter experiences the shock heating. The smaller density implies that the pressure at the surface of the inner core is smaller, and hence, the work exhausted by the inner core in converting the oscillation energy to the infalling outer envelop is smaller. Accordingly, the amplitudes of the bounce and the subsequent oscillation of the inner core become larger. Also, the equation of state “c” is “stiffer” than “b” in the (higher) density range between $\rho \approx 1.0 \times 10^{14}$ and $\approx 2 \times 10^{15}$ g/cm³ (cf. Figure 1). This also contributes to generating stronger shock waves. Because of these effects, the smaller value of ρ_{nuc} results in the larger threshold mass for the prompt black hole formation.

4. Effects of the rotation

As the value of q increases, the threshold mass for the prompt black hole formation becomes larger because the effect of the rotation effectively supplies additional pressure to the iron core and reduces the amount of matter falling into the central region. The threshold mass may be written approximately as a quadratic form [44]: $M_{\text{threshold}} = kq^2 + M_0$, where M_0 is the threshold mass for the spherical case. This reflects that the rotational kinetic energy (or the centrifugal force) depends on q^2 . Assuming this form of the threshold mass, we approximately draw the threshold curves in Fig. 6. It is found that the rotational effect increases the threshold mass by $\lesssim 15\text{--}25\%$ for $q \sim 1$. This value is comparable with the amplification factor of the maximum mass for rigidly rotating neutron stars in equilibrium [67].

The coefficient, k , depends on the strength of the shock and the adopted equation of state. The threshold mass for the prompt black hole formation at the maximum value of q is larger for the models with the smaller value of ρ_{nuc} as discussed in the previous subsection (compare models with equations of state b and c in Table IV). However, the dependence of the threshold mass at the maximum value of q on Γ_1 is not very simple. Comparing models with equations of state a and “b,” the black hole is more liable to be formed with equation of state “a,” i.e., for the *larger* value of Γ_1 . On the other hand, comparing models with equations of state “b” and “d,” no difference is found in the present numerical study. This is because the process of the black hole formation for models with $\Gamma_1 = 1.32$ is significantly different from those with $\Gamma_1 = 1.30$ and 1.28 , as described in Sec. IV B 2.

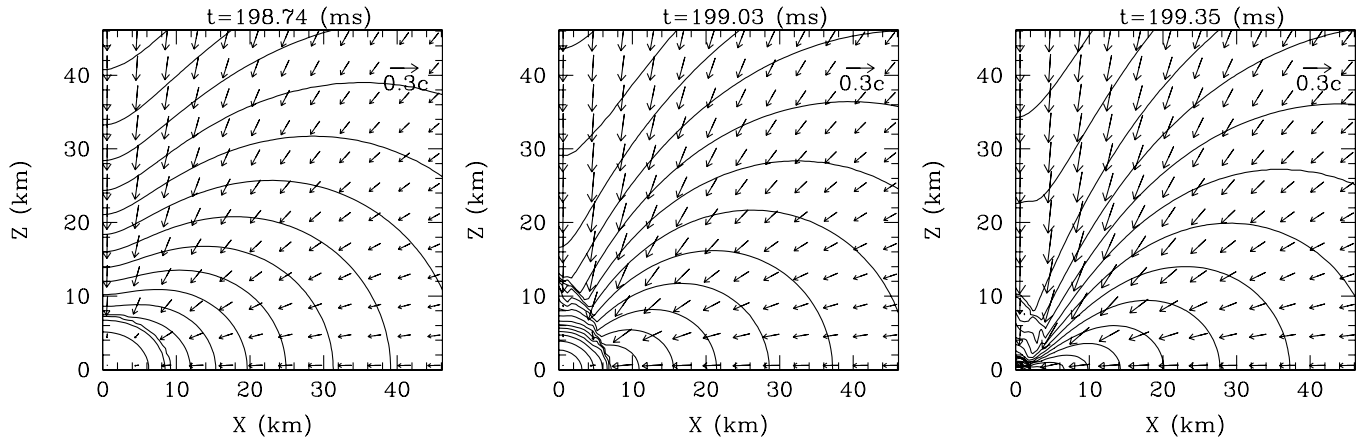


FIG. 9. The same as Fig. 7 but for model F5 with the equation of state “a,” at $t = 198.74, 199.03,$ and 199.35 ms. The thick solid curve in the last panel denotes the location of the apparent horizon.

To see the effect of the rotation on the collapse dynamics in more detail, in Figs. 9 and 10, we display the snapshots of the density contour curves and velocity vectors at selected time slices for models F5a and F5b. For these models, the value of q is nearly maximum among the rigidly rotating initial models of a given mass. For model

F5a, the collapse proceeds more rapidly in the direction of rotational axis (z axis) than in the equatorial plane during the infall phase. This is because the centrifugal force is stronger in the equatorial plane than around the z axis (see the first panel of Fig. 9). Accordingly, the collapsing inner region is deformed to be an oblate shape. As the collapse

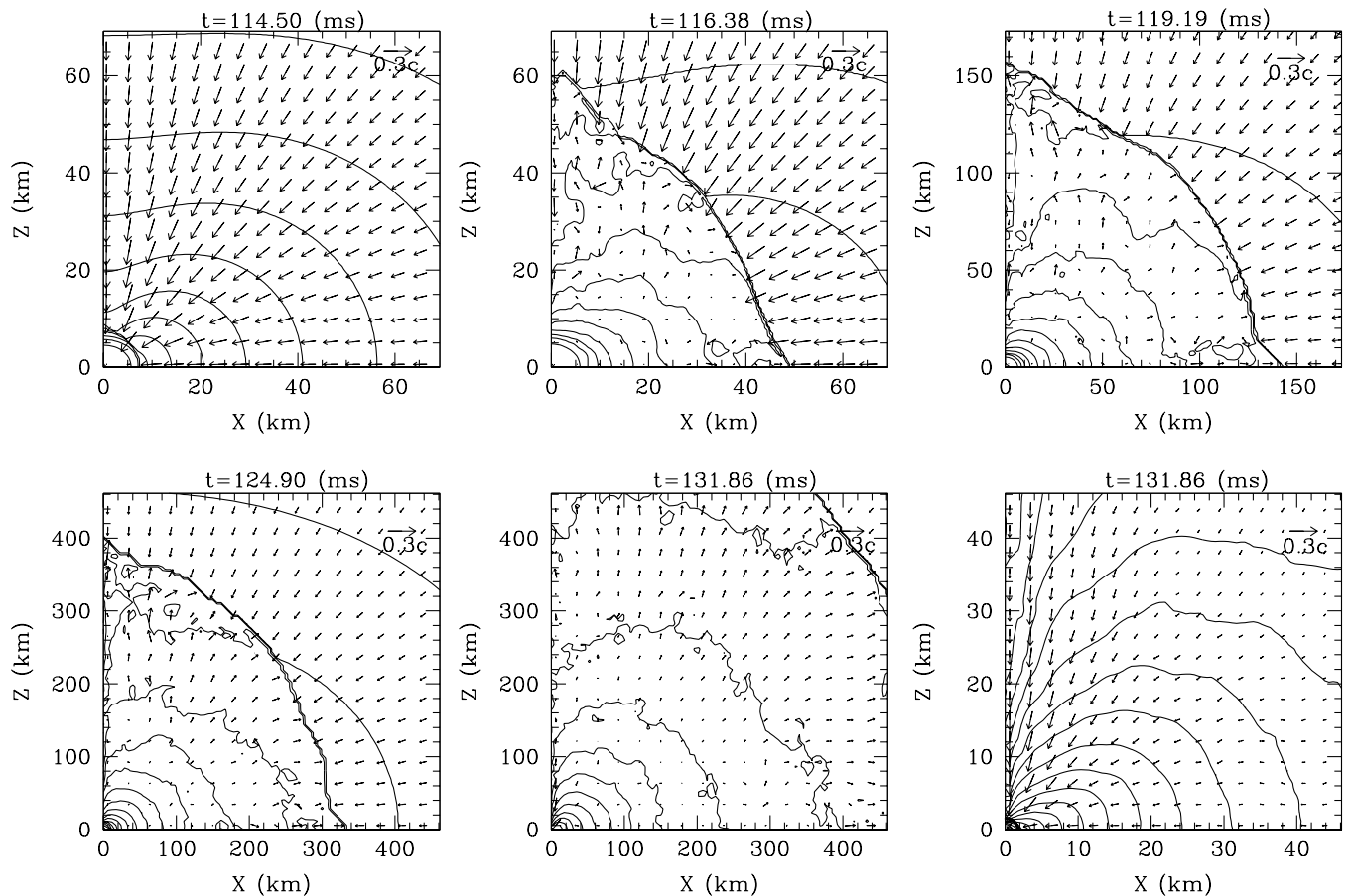


FIG. 10. The same as Fig. 7 but for model F5 with the equation of state “b,” at $t = 114.50, 116.38, 119.19, 124.90,$ and 131.86 ms. The thick solid curve in the last panel denotes the location of the apparent horizon.

proceeds, the density contour in the outer part of the inner core is deformed to be a concave structure. At the bounce, this leads to formation of a steep density gradient along the rotational axis (see the second panel of Fig. 9). This would result in stronger shock waves along the rotational axis than in the equatorial plane. For model F5a, however, the mass of the inner core at the bounce is so large that the strong gravitational attraction force prevents the shock from being propagated. Consequently, the inner core promptly collapses to a black hole. On the other hand, for less massive cases, shock waves propagate outward. In the shock propagation, this asymmetry generates anisotropic shocks (see also Sec. IV D).

For model F5b, shock waves propagate outward since the mass of the inner core at the bounce is smaller than the maximum allowed mass due to the smaller value of Γ_1 . In this case, however, the density gradient along the z axis is not so steep as that for model F5a (see the first panel of Fig. 10), although the mass and the angular momentum of the progenitor are identical between F5a and F5b. As a result, the asymmetry in the shock front is small (see the second to fourth panels of Fig. 10). The reason is that the mass of the inner core at the bounce is smaller for model F5b. For rigidly rotating initial models, the centrifugal force is stronger for larger cylindrical radius, and hence, the smaller mass of the inner core implies that the effect of rotation is less important.

For model F5b, the shock is strong enough to reach the surface of the iron core (see the fifth panel of Fig. 10). However, in a region behind the shock, the fluid elements (in particular) around the rotational axis fallback into a protoneutron star formed at the center, and eventually, the protoneutron star collapses to a black hole (see the last panel in Fig. 10). This illustrates that a black hole may be formed in a rather long time scale even for models in which the black hole is not formed promptly, if the progenitor is rotating.

TABLE V. Summary of the final outcome in the iron core collapse with differentially rotating initial models. The adopted equation of state is type b for all the cases; i.e., $(\Gamma_1, \Gamma_2, \rho_{14}) = (1.3, 2.5, 2.0)$.

Model	K_0 (cgs)	A	M_{ADM}/M_\odot	q	outcome
D20d1b	7.0×10^{14}	1.0	2.437	0.647	BH
D22d1b	7.0×10^{14}	1.0	2.441	0.698	BH
D23d1b	7.0×10^{14}	1.0	2.445	0.746	no BH
D25d1b	7.0×10^{14}	1.0	2.450	0.791	no BH
D15d05b	7.0×10^{14}	0.5	2.424	0.440	BH
D17d05b	7.0×10^{14}	0.5	2.430	0.541	BH
D20d05b	7.0×10^{14}	0.5	2.437	0.626	no BH
D25d05b	7.0×10^{14}	0.5	2.444	0.702	no BH
H5d1	8.0×10^{14}	1.0	3.019	0.978	BH
H5d05	8.0×10^{14}	0.5	3.020	0.941	no BH

5. Effects of differential rotation

Table V shows the outcomes of the collapse for all of differentially rotating initial models listed in Table III. In the simulation for differentially rotating models, we only adopt the equation of state ‘‘b.’’ Model D25d1 with $A = 1.0$ does not form a black hole, while its rigidly rotating counterpart D25 for which the mass and the angular momentum are approximately the same as those of D25d1 collapses to a black hole. For differentially rotating model D20d05 for which $A = 0.5$, and the mass and the angular momentum are slightly smaller than those for rigidly rotating model D2, black hole is not formed. For $A = 0.5$, black hole is not formed promptly even from a very massive initial model H in which $M_{\text{ADM}} \approx 3.0M_\odot$ (cf. Table V). These indicate that the black hole is less liable to be formed promptly for the higher degree of differential rotation.

The results found here are quite reasonable since with the decrease of A , the angular velocity in the inner region increases. To clarify this effect in a more quantitative manner, we generate Fig. 11, which shows the spin parameter distribution $q_*(j)$ defined by Eq. (14). First, note that a black hole is formed for models D25 and D22d1 but not for D3 and D25d1 with the equation of state ‘‘b.’’ The two dotted curves in Figs. 11(a) and 11(b) denote $q_*(j)$ of these two models D3b (upper dotted curve) and D25b (lower dotted curve), respectively. The solid and dashed curves in Fig. 11(a) denote $q_*(j)$ for models D25d1 and D22d1 for which $A = 1.0$. Although the total value of the spin parameter of the differentially rotating iron cores of D25d1 ($q = 0.791$) is smaller than that for rigidly rotating model D3 ($q = 0.888$), the value of q_* around the central region ($m_*(j) \leq M_*/2$) exceeds that of D3. As shown in [12] in detail, the value of q_* around the center plays a crucial role in determining the criterion for prompt black hole formation; i.e., the iron core with a larger value of q_* around the center is less liable to collapse to a black hole. Therefore, it is reasonable that black hole is not formed for model D25d1. On the other hand, the value of q_* around the center for model D22d1 ($q = 0.698$) is as large as that for model D25 around the central region. This implies the rotational centrifugal force is not strong enough to prevent the iron core from collapsing to a black hole.

Figure 11(b) shows $q_*(j)$ for models D20d05 (solid curve) and D17d05 (dashed curve) with $A = 0.5$. A black hole is not formed for D20d05 while it is formed for D17d05. Figure 11(b) clarifies that the spin parameter distribution is flatter with the smaller value of A . Therefore, the values of the global spin parameter q for $A = 0.5$ are much smaller than those of the rigidly rotating counterparts. On the other hand, the value of q_* around the central region becomes larger. As a result, black hole formation is more effectively prevented. This quantitatively indicates that the threshold mass for the prompt black hole formation is larger for models with larger degree of differential rotation.

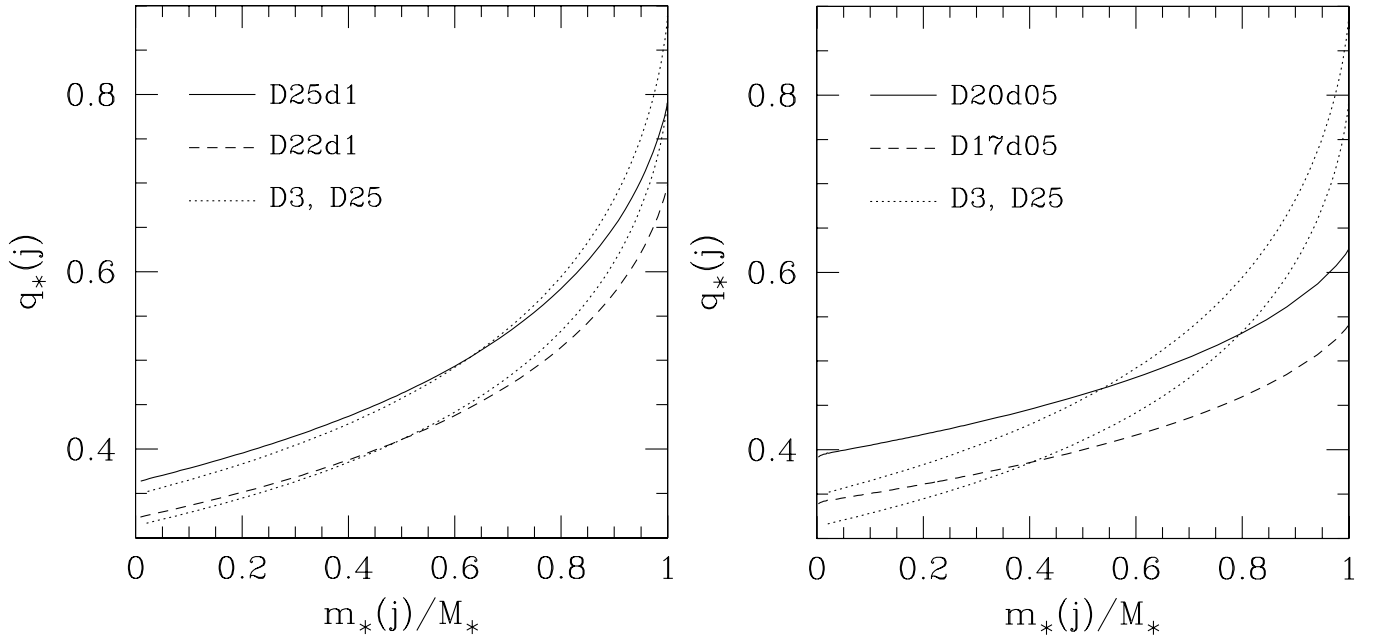


FIG. 11. The spin parameter distribution inside differentially rotating iron cores of (a) D25d1 (solid curve) and D22d1 (dashed curve); (b) D20d05 (solid curve) and D17d05 (dashed curve). The two dotted curves in both figures denote the spin parameter distribution for the rigidly rotating models D3 (upper dotted curve) and D25 (lower dotted curve). Note that for model D3b, a black hole is formed promptly, while for D25b, a neutron star is formed.

C. Prediction of the final system

Because of the assumption that the viscous effect is negligible during the collapse, the specific angular momentum $j = \hat{u}_\varphi$ of each fluid element is conserved in the axisymmetric system and so do the functions $m_*(j)$ and $J_*(j)$. Using this fact, the final outcome after the black hole formation can be predicted [10,12,19].

Let us consider innermost stable circular orbit (ISCO) around the growing black hole located at the center. Assuming that a fluid element around a black hole is approximately in a circular orbit, it will fall into the seed black hole eventually if its value of j is smaller than that at the ISCO (j_{ISCO}). The value of j_{ISCO} depends on the mass and the angular momentum of the black hole and changes as the ambient fluid elements accrete onto the black hole. If j_{ISCO} increases as a result of the accretion, the more ambient fluid elements will fall into the black hole. On the other hand, if j_{ISCO} decreases during the accretion, no more fluid element will fall into the black hole, and as a result, the dynamical growth of the black hole will terminate. Therefore, if j_{ISCO} has a maximum (hereafter denoted as $j_{\text{ISCO: max}}$), the black hole will grow until j reaches $j_{\text{ISCO: max}}$. Namely, it is reasonable to expect that the final values of the mass and the spin parameter of the black hole will be

$$M_{\text{BH}} \approx m_*(j_{\text{ISCO: max}}), \quad (36)$$

$$q_{\text{BH}} \approx q_*(j_{\text{ISCO: max}}). \quad (37)$$

with the disk mass $M_{\text{ADM}} - m_*(j_{\text{ISCO: max}})$.

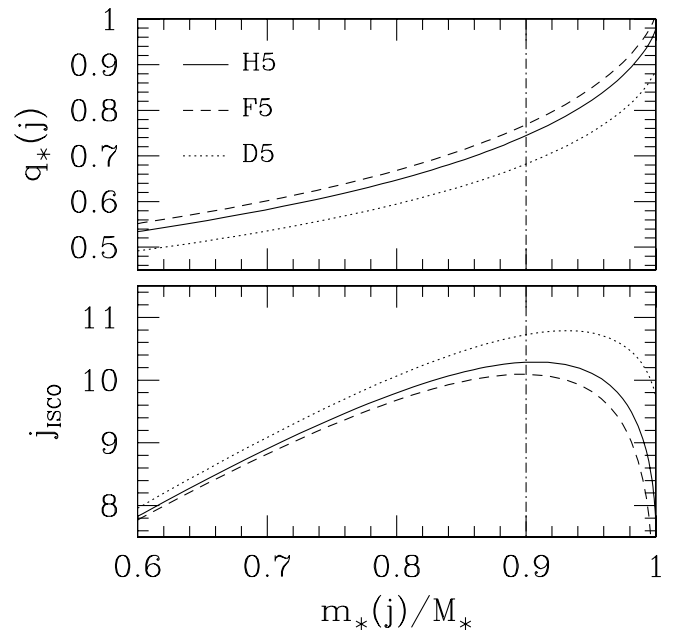


FIG. 12. The distribution of $q(j)$ (top panel) and the value of j_{ISCO} as a function of $m_*(j)/M_*$ for models H5 (solid curve), F5 (dashed curve), and D3 (dotted curve). The dotted dashed vertical line denotes $m_*(j)/M_* = 0.9$ where j_{ISCO} for F5 takes the maximum value approximately.

To estimate the value of j_{ISCO} , we assume that the spacetime metric can be instantaneously approximated by that of a Kerr spacetime of the mass $m_*(j)$ and the spin $q_*(j)$. On these approximations, we can compute j_{ISCO} of a growing black hole as [13,72],

$$j_{\text{ISCO}} = \frac{\sqrt{m_*(j)r_{\text{ISCO}}}(r_{\text{ISCO}}^2 - 2q_*(j)m_*(j)\sqrt{m_*(j)r_{\text{ISCO}}} + (q_*(j)m_*(j))^2)}{r_{\text{ISCO}}(r_{\text{ISCO}}^2 - 3m_*(j)r_{\text{ISCO}} + 2q_*(j)m_*(j)\sqrt{m_*(j)r_{\text{ISCO}}})^{1/2}}, \quad (38)$$

where

$$\begin{aligned} r_{\text{ISCO}} &= m_*(j)[3 + Z_2 \\ &\quad - \{(3 - Z_1)(3 + Z_1 + 2Z_2)\}^{1/2}], \\ Z_1 &= 1 + [1 - q_*(j)^2]^{1/3}[\{1 + q_*(j)\}^{1/3} \\ &\quad + \{1 - q_*(j)\}^{1/3}], \\ Z_2 &= [3q_*(j)^2 + Z_1^2]^{1/2}. \end{aligned}$$

In Fig. 12, we show the quasilocal spin parameter distributions inside the iron core, defined by Eq. (14), and the value of j_{ISCO} evaluated by Eq. (38) for models H5, F5, and D3. As described above, the dynamical evolution of the formed black hole will terminate when j_{ISCO} reaches a local maximum. Then, the mass, M_{BH} , and spin, q_{BH} , of the the dynamically evolved black hole are given by Eqs. (36) and (37).

Figure 12 indicates that for model F5 and H5, the inner region collapse to form a black hole of $M_{\text{BH}}/M_* \approx 0.90$ and $q_{\text{BH}} \approx 0.76$. On the other hand, the matter in the outer region of high specific angular momentum will form a massive disk of $M_{\text{disk}}/M_* \approx 0.10$ around the black hole. Similarly, for model D3, a black hole of $M_{\text{BH}}/M_* \approx 0.93$ and $q_{\text{BH}} \approx 0.73$ will be formed. Such a rapidly rotating black hole surrounded by a massive disk is one of the promising candidates for the central engine of the long-duration gamma-ray bursts [7–9].

Although the above prediction is quite reasonable [12], confirmation of this prediction requires to carry out a simulation until the black hole plus disk system is formed. To accomplish this, the so-called black hole excision techniques are required. For the case of the collapse with stiff ($\Gamma = 2.0$) equations of state, we have confirmed it possible to continue the simulation more than $\sim 100M$ after the formation of black hole by using techniques based on the so-called simple excision developed by Alcubierre and Brüggmann [73]. We plan to wrestle with the confirmation of the above prediction by extending the techniques to the collapse with soft equations of state.

D. Proton-neutron star formation

1. Dependence of explosion on the equations of state

As discussed in the previous subsections, the dynamics of the collapse and the threshold mass for the prompt black hole formation depend sensitively on the equations of state.

In the case of neutron star formation, we also find that features of the explosion depend sensitively on the equations of state. We illustrate this fact focusing on rapidly rotating model D5 in which black hole is not formed promptly irrespective of the equations of state.

In Fig. 13, we display the contour plots for model D5a. For the collapse with the equation of state ‘‘a’’ which is stiff in the subnuclear density (with larger value of Γ_1) while soft in the supranuclear density (with smaller value of Γ_2), the steep density gradient is formed around the rotational axis of the inner core. On the other hand, such steep gradient is not formed around the equatorial plane (see the second panel of Fig. 13). Because of the steep gradient, strong shock waves are generated along the rotational axis. Consequently, a jetlike explosion is seen (see the third panel of Fig. 13). The explosion velocity in the direction of the rotational axis is much larger than that in the equatorial plane (see the fourth and fifth panels of Fig. 13): The maximum speed becomes $\approx 0.8c$ around the rotational axis near the shock. Thus, the shock wave reaches the surface of the iron core much more quickly (see the last panel of Fig. 13). At this time, a funnel structure is formed around the rotational axis.

The structure of bipolar shock waves depends on mass of progenitor. For model A5a in which $M_{\text{ADM}} \approx 1.97M_\odot$, a steep density gradient is also formed along the rotational axis (see Fig. 14), but it is formed only in narrower region than that for model D5a (compare the first panel of Fig. 14 and the second panel of Fig. 13). Reflecting this result, the structure of the shock front is sharper than that for model D5a and is deformed to be spearlike (compare the second panel of Fig. 14 and the third panel of Fig. 13).

Such bipolar and energetic supernova explosion is required to explain the observations of several hypernovae, which are suggested to be associated with a gamma-ray burst [6,74–77]. Indeed, the energetic explosion along the rotational axis is preferable to avoid the baryon-loading problem in the fireball model of the gamma-ray bursts [9]. The present results suggest that the collapse of rapidly rotating iron cores of $M \gtrsim 2M_\odot$ with a class of equations of state similar to a is preferable for realizing such a state.

To see the dependence of the features of the explosion on the equations of state, we also display the contour plots for models D5b and D5d in Figs. 15 and 16. As the first panel of these figures show, the magnitude of the density gradient along the rotational axis is not very different from that in the equatorial plane, and hence, structure of the shock is

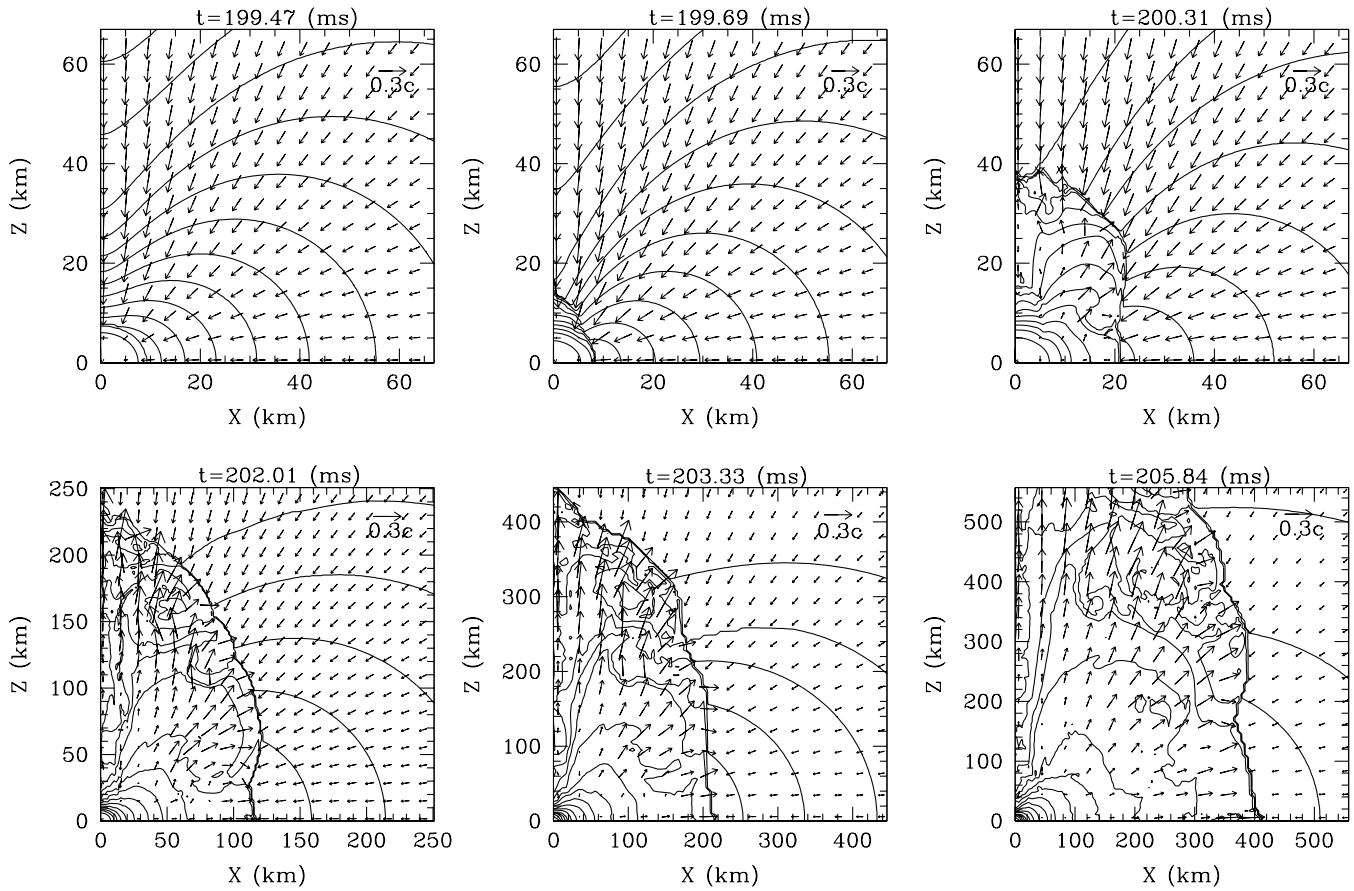


FIG. 13. The same as Fig. 7 but for model D5 with the equation of state “a,” at $t = 199.47, 199.69, 200.31, 202.01, 203.33,$ and 205.84 ms.

not very aspherical (see the second panel of the Figs. 15 and 16).

The shock for model D5b is strong enough to quickly propagate through the outer core, sweeping the matter falling into the shock. For model D5d, on the other hand, the shock is not as strong as that for D5b, and hence, the propagation speed is slow. Also, the density gradient

formed around the shock is not very different between along the rotational axis and in the equatorial plane, and hence, the structure of the shock becomes eventually oblate (not prolate) due to the effect of the rotation (see the third panel of Fig. 16). As the matter behind the shock falls and beats the protoneutron star at the center, it oscillates and the shocks are formed continuously. Thus, the shocks

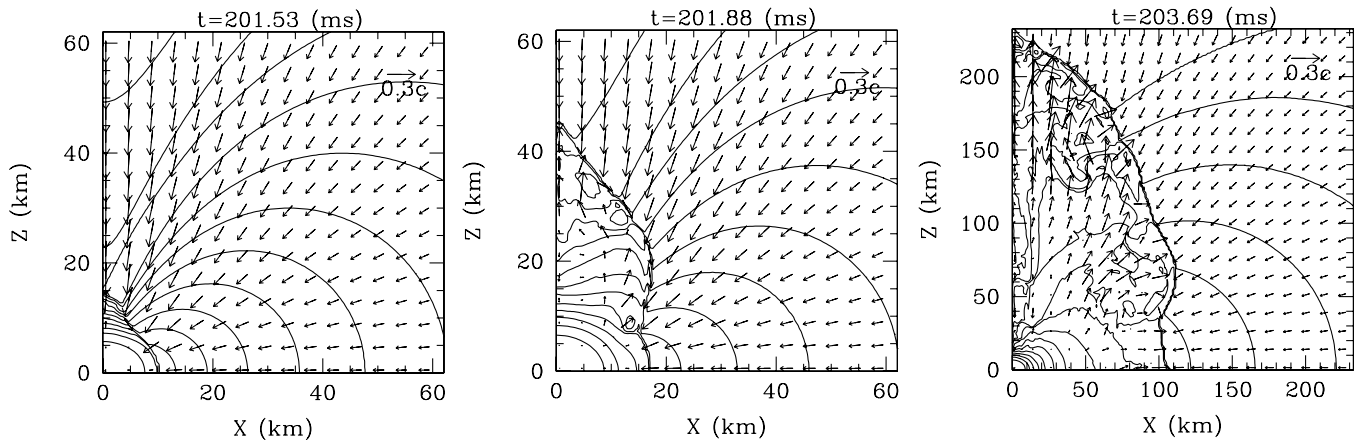


FIG. 14. The same as Fig. 7 but for model A5 with the equation of state “a,” at $t = 201.53, 201.88,$ and 203.69 ms.

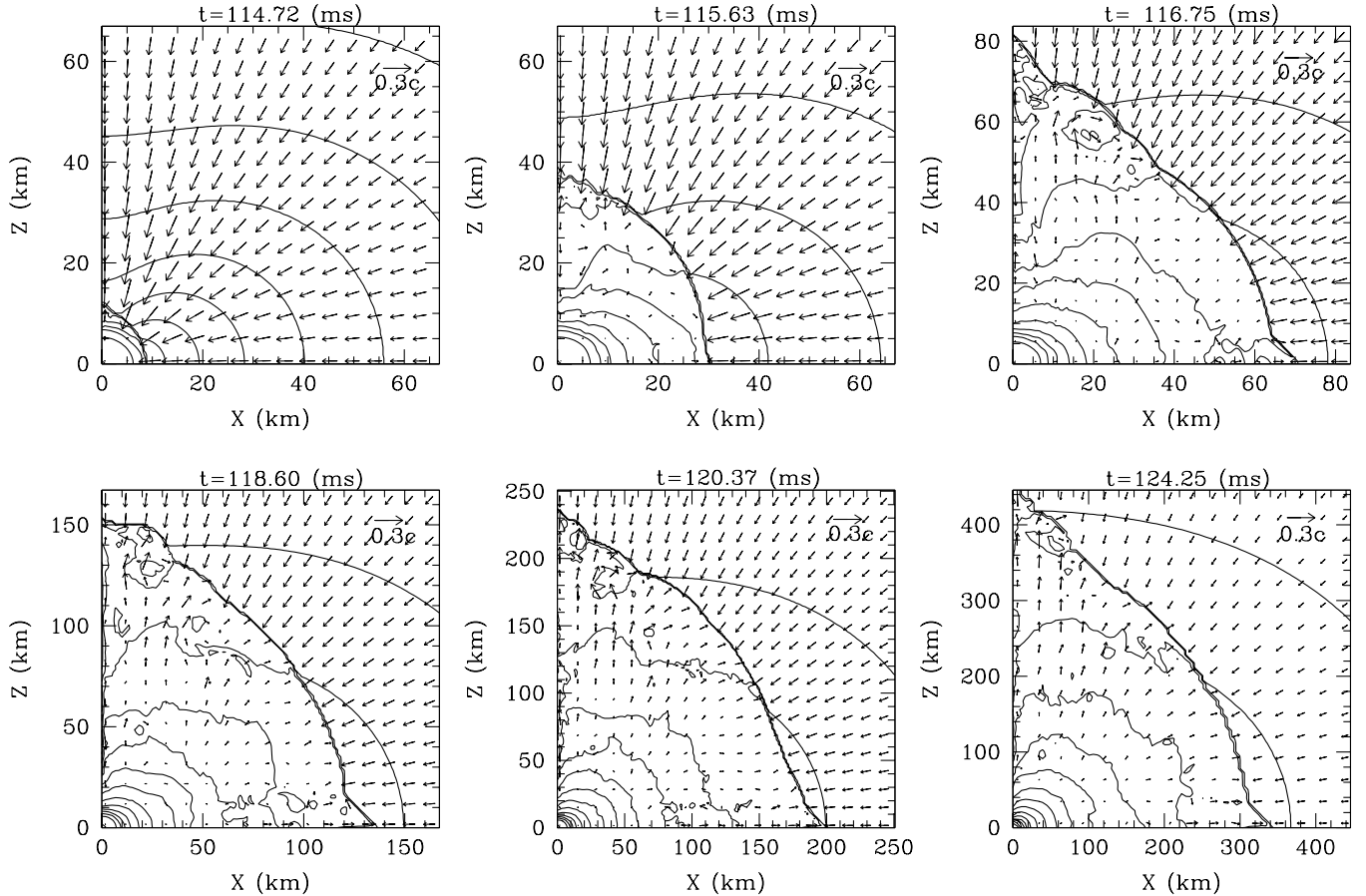


FIG. 15. The same figure as Fig. 7 but for model D5 with the equation of state “b,” at $t = 114.72, 115.63, 116.75, 118.60, 120.37,$ and 124.25 ms.

propagates outward and helps sweeping the infalling matter outward (see the fourth and fifth panels of Fig. 16). The features found for models D5b and D5d are not found in model D5a. This fact implies that the explosion mechanism depends sensitively on the equations of state for rapidly rotating iron core collapse.

It should be also mentioned that the bipolar explosion has not been found in the previous study [36] in which the same parametric equation of state with $(\Gamma_1, \Gamma_2) = (1.32, 2.5)$ and smaller core mass of $1.5M_\odot$ is adopted. (Note that this equation of state is stiffer in supranuclear density than the equation of state a of the present paper). This fact implies that an equation of state with not only a large value of $\Gamma_1 (= 1.32)$ but also a small value of $\Gamma_2 \leq 2.25$ may be required for producing the bipolar explosion.

2. Rotational profile of the protoneutron star

In this subsection, we present the rotational profiles of the inner region during the collapse and consider the possibility for the onset of the nonaxisymmetric instabilities. Figs. 17–20 show the angular velocity profile along the x axis at selected time slices for models D5a, D5b, D5c, and D5d, respectively. The first panels of Figs. 17–20 show

the angular velocity profile around the bounce phase. As the collapse proceeds, the angular velocity around the central region increases toward the maximum value, Ω_{\max} , achieved at the bounce. The values are $\Omega_{\max} \approx 8000, 10000, 6000,$ and 7500 s^{-1} for models D5a, D5b, D5c, and D5d, respectively, (see dotted lines in the first panels). The inner core at the bounce, when the maximum angular velocity is achieved, is approximately rigidly rotating irrespective of the equations of state, although the fluid elements outside the inner core is differentially rotating as a whole. These results indicate that the differential rotation is not enhanced in the inner core during the infall and bounce phases.

The second panels of Figs. 17–20 show the angular velocity profiles in the ring-down phase, from which we find that differential rotation is enhanced in the ring-down phase due to the oscillation of the protoneutron star and the infall of the fluid elements of high specific angular momentum from the outer region. However, the degree of the differential rotation is not very high. This feature is also found in a Newtonian simulation [33]. These panels also indicate that the amplitude of the oscillation of the angular velocity is larger for models with the equation of state “c.”

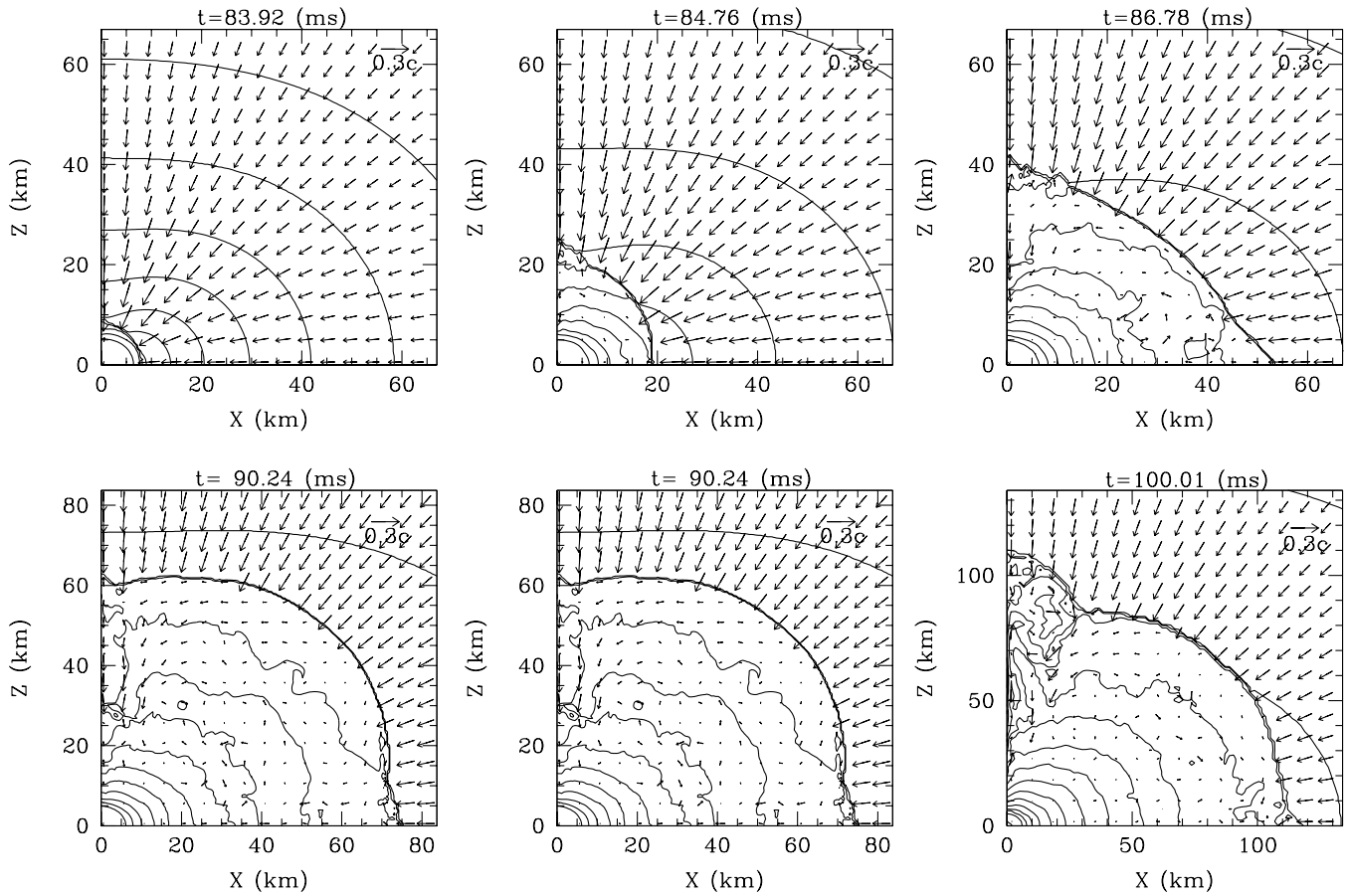


FIG. 16. The same as Fig. 7 but for model D5 with the equation of state “d,” at $t = 83.92, 84.76, 86.78, 88.92, 90.24,$ and 100.01 ms.

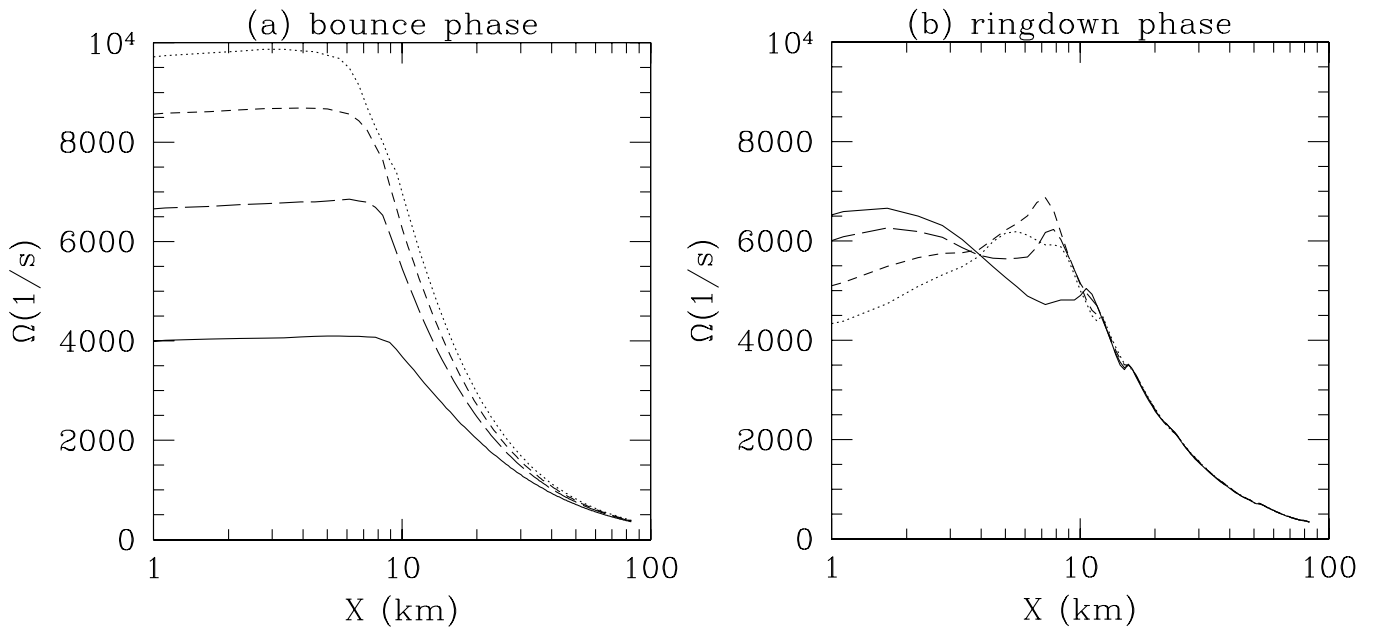


FIG. 17. The angular velocity profile inside the iron core along the x axis for model D5a at selected time slices: (a) at the bounce phase of $t = 199.43$ (solid curve), 199.62 (long dashed curve), 199.73 (dashed curve), and 199.86 ms (dotted curve); (b) at the ringdown phase of $t = 206.49$ (solid curve), 206.75 (long dashed curve), 206.94 (dashed curve), and 207.12 ms (dotted curve).

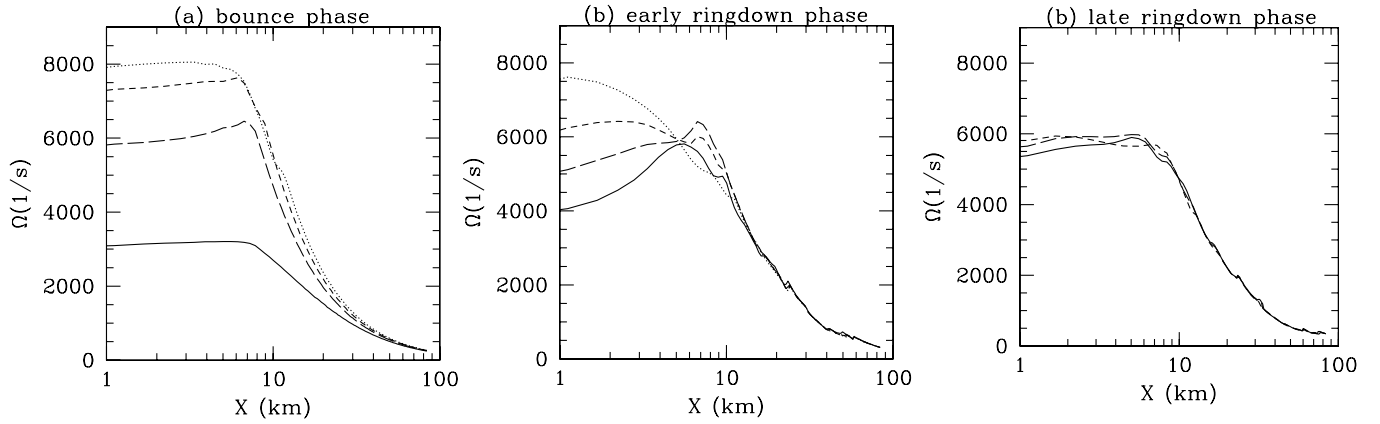


FIG. 18. The same as Fig. 17 but for model D5b at selected time slices: (a) at the bounce phase of $t = 114.39$ (solid curve), 114.61 (long dashed curve), 114.74 (dashed curve), and 114.87 ms (dotted curve); (b) at the early ring-down phase of $t = 118.86$ (solid curve), 119.16 (long dashed curve), 119.29 (dashed curve), and 119.53 ms (dotted curve); (c) at the late ring-down phase of $t = 122.06$ (solid curve), 122.36 (long dashed curve), 122.67 ms (dashed curve).

This is due to the fact that the amplitude of the oscillation of the protoneutron star is larger as described in Sec. IV B 3.

In the post-bounce oscillation phase, the oscillation of the protoneutron star gradually damps. The damping is caused by the compressional work of the protoneutron star to the infalling matter from the outer envelop. As a result of damping, a quasistationary protoneutron star rotating rapidly at the period $P \equiv 2\pi/\Omega \sim 1$ ms is eventually formed. Note that inner region of the formed protoneutron star is rigidly rotating (see the third panel of Fig. 18).

To infer the nonaxisymmetric stabilities, we estimate the value of T_{rot}/W at the bounce. Note that in general relativity, there is no unique definition for T_{rot}/W for dynamical spacetimes. In this paper, we define the rotational kinetic energy, T_{rot} , and the gravitational potential energy, W , for dynamical spacetime by

$$T_{\text{rot}} \equiv \frac{1}{2} \int d^3x \rho_* \hat{u}_\varphi v^\varphi, \quad (39)$$

$$W \equiv T_{\text{total}} + U, \quad \text{where } U \equiv \int d^3x \rho_* \varepsilon. \quad (40)$$

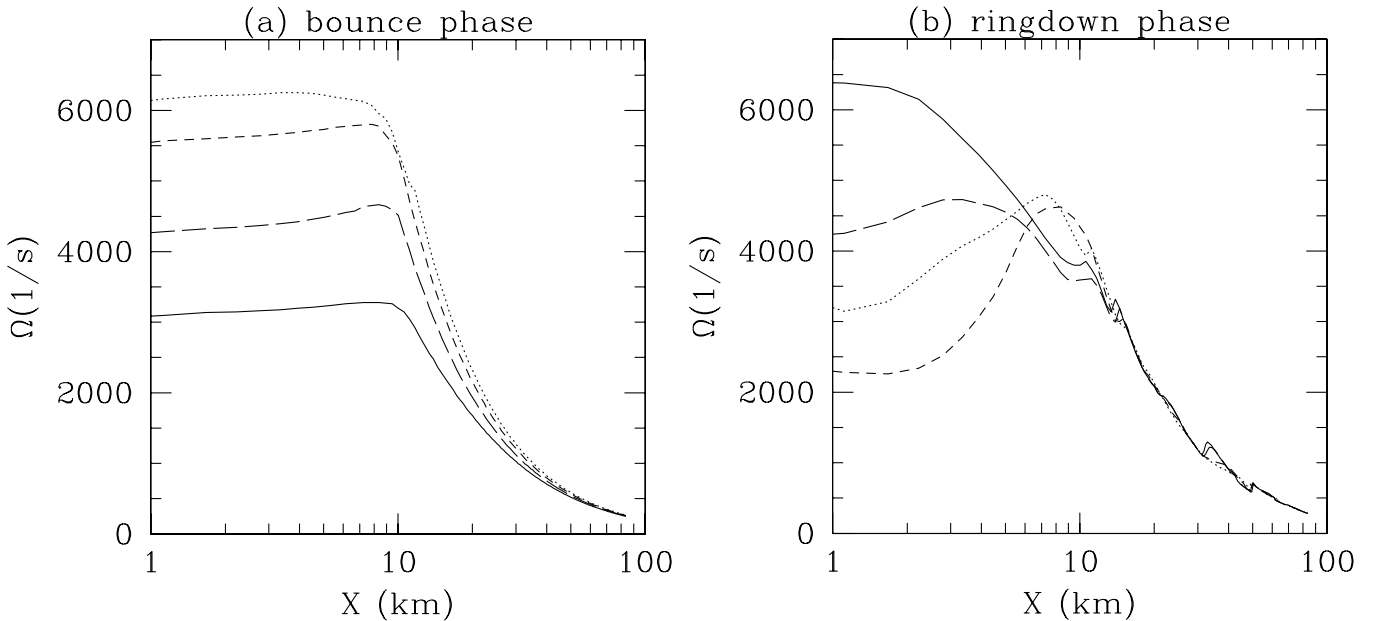


FIG. 19. The same as Fig. 17 but for model D5c at selected time slices: (a) at the bounce phase of $t = 114.46$ (solid curve), 114.59 (long dashed curve), 114.72 (dashed curve), and 114.83 ms (dotted curve); (b) at the ring-down phase of $t = 120.96$ (solid curve), 121.11 (long dashed curve), 121.67 (dashed curve), and 121.97 ms (dotted curve).

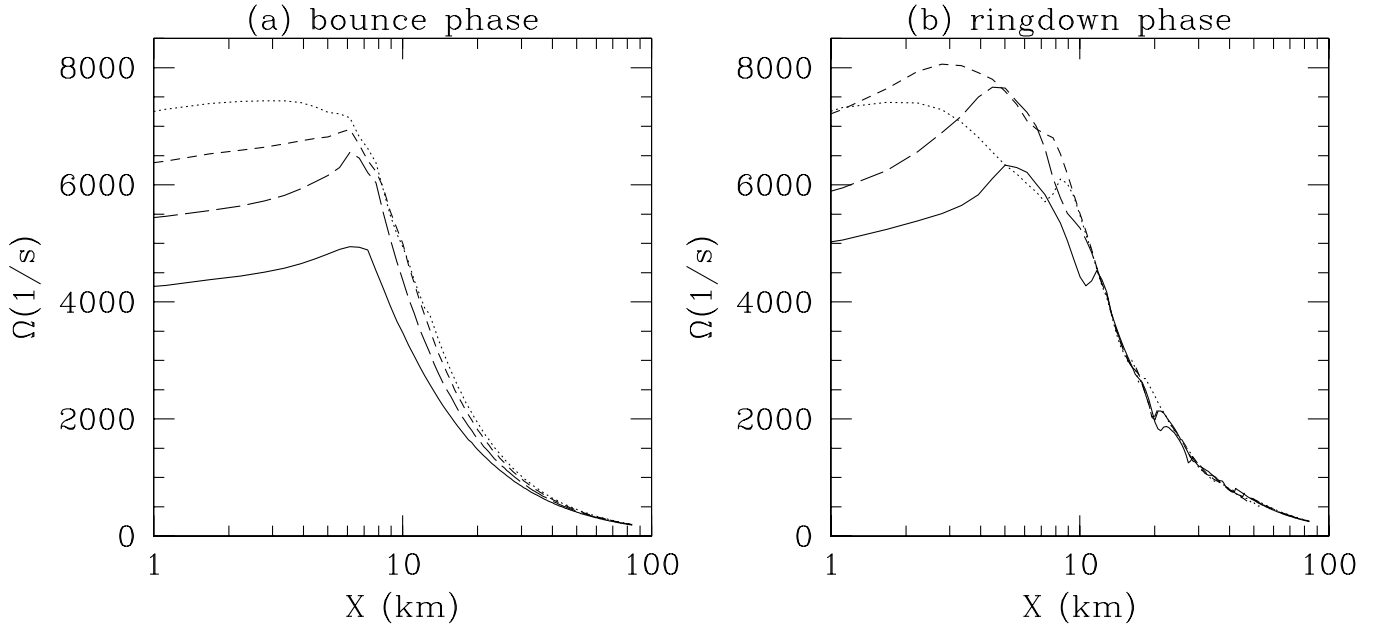


FIG. 20. The same as Fig. 17 but for model D5d at selected time slices: (a) at the bounce phase of $t = 83.78$ (solid curve), 83.91 (long dashed curve), 84.04 (dashed curve), and 84.15 ms (dotted curve); (b) at the ring-down phase of $t = 86.10$ (solid curve), 86.32 (long dashed curve), 86.51 (dashed curve), and 86.71 ms (dotted curve).

To define W , we use the fact that $M_{\text{ADM}} \approx M_* - W + T_{\text{total}} + U$ and $M_* \approx M_{\text{ADM}} \cdot T_{\text{total}}$ denotes a total kinetic energy. Unfortunately, we do not know the appropriate definition for T_{total} . However, as far as configurations at the maximum compression and at a final relaxed state are concerned, the rotational kinetic energy T_{rot} is nearly equal to T_{total} , and thus, T_{total} in Eq. (40) may be replaced by T_{rot} . In this definition, T_{rot}/W will give slightly overestimated values in other stages such as the infall phase. The value of T_{rot}/W at the bounce is ≈ 0.10 and ≈ 0.13 for models D5b and D5a. These values are much smaller than the plausible critical value of T_{rot}/W for the onset of the dynamical instability $T_{\text{rot}}/W \approx 0.24\text{--}0.25$ for nearly rigidly rotating stars [65,68,78], and hence, the inner core at the bounce and formed protoneutron star is unlikely to be unstable against nonaxisymmetric perturbations in the dynamical time scale. However, these values are as large as the critical value of T_{rot}/W for the secular instabilities driven by gravitational wave emission [65,79,80], or driven by viscosity [65,81]. Therefore, the formed protoneutron star may be unstable against nonaxisymmetric perturbations in secular time scales $\gg 100$ ms.

A sufficiently rapidly and differentially rotating iron core may collapse to form a protoneutron star of $T_{\text{rot}}/W \geq 0.25$ and become unstable against nonaxisymmetric perturbations. Such a rotating nonaxisymmetric object will be a strong gravitational wave emitter. In a companion paper [38], we study conditions for the onset of the dynamical instabilities in three-dimensional numerical simulation in full general relativity. We find that the dynamical instabilities set in only for the case that the progenitor is highly

differentially rotating with $A \lesssim 0.1$. Thus, the assumption of axial symmetry in this paper is justified.

E. Gravitational waves

1. Gravitational waveforms

Gravitational waveforms are computed in terms of the quadrupole formula described in Sec. II C. As illustrated in a previous paper [55], approximate gravitational waveforms can be computed even for highly relativistic, highly oscillating, and rapidly rotating neutron stars using the quadrupole formula except for systematic underestimate of the amplitudes of $O(M/R)$. In the case of protoneutron star formation, gravitational waves are emitted mainly by its oscillation. Thus, with the quadrupole formula, it is possible to approximately compute gravitational waveforms emitted during rotating iron core collapse to a protoneutron star.

In Figs. 21–23, gravitational waves for models D2–D5 with equations of state “a,” “b,” and “d” are shown. The gravitational waveforms during the black hole formation evaluated by the quadrupole formula are also presented together for models D3a, D2b, and D2d. We note that from $A_2 = \ddot{I}_{zz} - \ddot{I}_{xx}$, the amplitude of gravitational waves at a distance of r from the source is calculated by

$$h \approx 3 \times 10^{-20} \left(\frac{A_2}{1000 \text{ cm}} \right) \left(\frac{10 \text{ kpc}}{r} \right) \sin^2 \theta, \quad (41)$$

where θ denotes the angle between the line of sight and the rotational axis, and $\langle \sin^2 \theta \rangle = 2/3$. Thus, the typical amplitude is $\sim 2 \times 10^{-20}$ for a event at the galactic center.

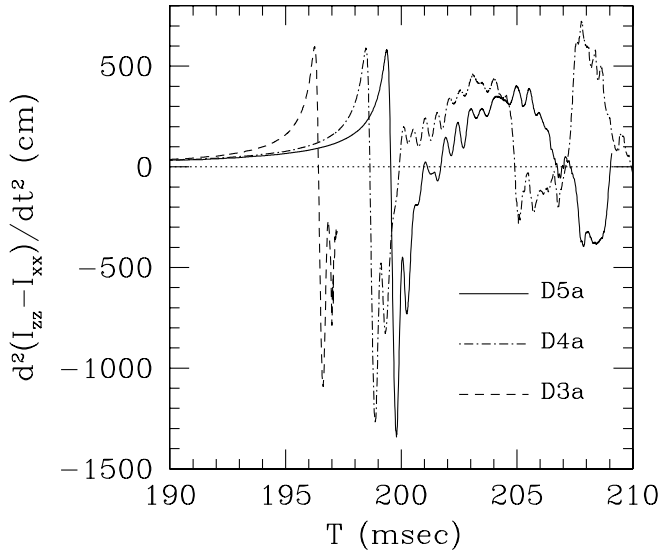


FIG. 21. Gravitational waveforms computed by the quadrupole formula described in Sec. II C for models D5a (solid curve) and D4a (dotted dashed curve), and D3a (dashed curve).

Figs. 21–23 show that the strong dependence of the dynamics of the collapse on the values of Γ_1 is reflected in the amplitude of gravitational waveforms. The following features are, in particular, worthy to note. First, the amplitudes of gravitational waves during the infall and bounce phases are smaller for the smaller value of Γ_1 (the larger value of $|\Gamma_1 - 4/3|$). The reason is that the smaller value of Γ_1 results in the smaller mass of the inner core at the bounce (cf. discussion in Sec. IV B 2). This feature agrees with that found in previous works [29,34,36].

Second, the time-averaged amplitudes of the gravitational waves in the ring-down phase are negative for mod-

els with equations of state “b” and “d” while positive for the model with “a.” This results from the difference of the dynamics in the infall phase. For the equations of state “a,” the matter collapses and bounces in a coherent manner, while for the equations of state “b” and “d,” in a less coherent manner. In the case “b” and “d,” therefore, the matter in the outer region infalling toward the center suppresses the oscillation of the protoneutron star. On the other hand, for models with “a,” such suppression does not work effectively because of the smaller-mass fraction in the outer region.

Third, the gravitational waveforms for rapidly rotating models with the equations of state a (models D4a and D5a in Fig. 21) are qualitatively different from those for others. The modulation of the gravitational waveforms are quite remarkable. This reflects the bipolar explosion, in which absolute value of \ddot{I}_{zz} is much larger than that of \ddot{I}_{xx} .

Fourth, the so-called “type-III” gravitational waveforms [29] are not found in any model. Previous studies have indicated that type-III waveforms are generated for a small value of $\Gamma_1 \sim 1.28$ [29,34,36]. In these waveforms, the amplitude of the first spike is significantly suppressed to the value $|\ddot{I}_{zz} - \ddot{I}_{xx}| \sim 30$ cm. This is because the mass of the protoneutron star at the bounce phase is very small for such small value of Γ_1 . In the present case, the mass of the adopted iron core is much larger than that for the previous studies [29,34,36]. As a result, the mass of the protoneutron star is not very small, and hence, the type-III gravitational waveforms are not generated.

For a given mass, the amplitude of gravitational waves is increased with the increase of the angular momentum in the present numerical results. However, this is not trivial result because of the following reasons. First, recall that the amplitude of gravitational waves is proportional to the

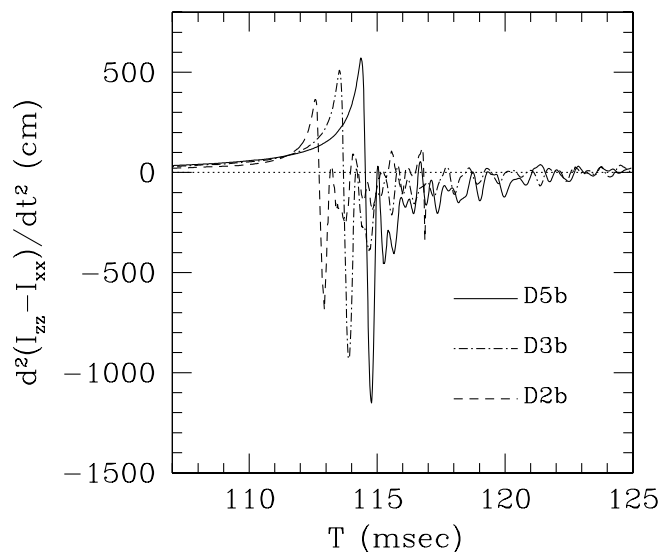


FIG. 22. The same as Fig. 21 but for models D5b (solid curve), D3b (dotted dashed curve), and D2b (dashed curve).

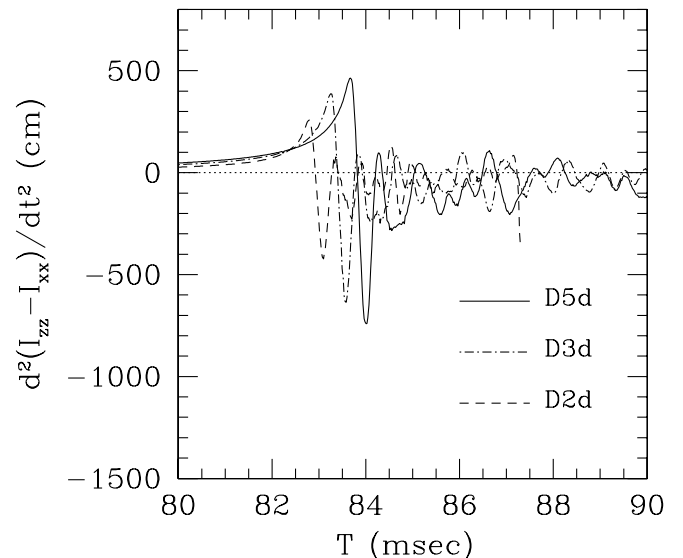


FIG. 23. The same as Fig. 21 but for models D5d (solid curve), D3d (dotted dashed curve), and D2d (dashed curve).

quadrupole moment ($|I_{zz} - I_{xx}|$) and the inverse square of the dynamical time scales, τ_{char} , of the system. The value of $|I_{zz} - I_{xx}|$ increases as the total angular momentum increases since the radius and the degree of deformation of the inner core become larger due to the increasing centrifugal force. On the other hand, the characteristic time scale becomes longer as the angular momentum of the inner core increases since the rotation effectively supplies additional pressure to the inner core and the collapse is decelerated. Thus, these two contrary effects may cancel each other with a certain value of spin parameter q , resulting in the saturation of the burstlike gravitational wave signals. Indeed, such saturation was found at $q \sim 1$ in previous Newtonian studies (e.g., [28]) since at such a large value of q , the iron core does not collapse to a sufficiently compact state. However, saturation is not found in the general relativistic studies [34,36]. This implies that the general relativistic gravity is strong enough to overcome the centrifugal force for the rigidly rotating case with $q \lesssim 1$. This effect also suppresses to yield type-II gravitational waves [34] which appear in the case that the centrifugal force is too strong for the iron core to reach the nuclear density.

In Fig. 24, we show gravitational waveforms for models B5b, D5b, and F5b to illustrate the dependence of them on the mass of the iron core. In the infall phase, the amplitude of gravitational waves is larger for the larger-mass model. This is quite natural since for the larger-mass model, the quadrupole moment of the inner cores are larger. On the other hand, the amplitude of the strong spike at the bounce saturates when the mass of the iron core reaches $\approx 2.5M_{\odot}$. The plausible reason is that the inner core shrinks to be so compact that the quadrupole moment is decreased significantly.

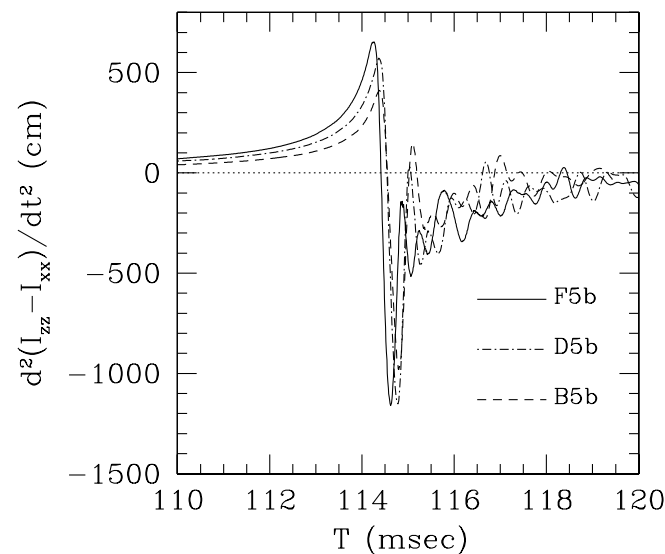


FIG. 24. The same as Fig. 21 but for models F5b (solid curve), D5b (dotted dashed curve), and B5b (dashed curve).

The effect of mass on the amplitude of gravitational waves can be analyzed by comparing the present results with the previous results in [36], in which collapse of the iron core of mass $M \approx 1.5M_{\odot}$ and rotational energy $T_{\text{rot}}/W \approx 0.009$ are studied. In [36], we found that the amplitudes of gravitational waves at the bounce are $|\ddot{I}_{zz} - \ddot{I}_{xx}| \approx 650\,200$, and 30 cm for models with $(\Gamma_1, \Gamma_2) = (1.32, 2.0)$, $(1.31, 2.5)$, and $(1.28, 2.5)$. These results should be compared with the present results for D5a, D5b, and D5d, in which $M \approx 2.5M_{\odot}$ and $T_{\text{rot}}/W \approx 0.009$ and the amplitudes of gravitational waves are $|\ddot{I}_{zz} - \ddot{I}_{xx}| \approx 1350$, 1200, and 750 cm, respectively. These values are larger than those found in [36] by factors of ≈ 2 , 6, and 25. Thus, with the increase of the mass, the amplitude is increased in a nonlinear manner. For $\Gamma_1 = 1.32$, the increase factor is small. The reason is that for this case, the inner core at the bounce becomes sufficiently large due to the coherence collapse in the infall phase, and the mass is close to the value for the saturation as mentioned above. For other cases, the increase factor is much larger. In particular, the increase factor for $\Gamma_1 = 1.28$ is outstanding. This is associated with the fact that the dynamics in the bounce phase qualitatively changes with the increase of mass. For $\Gamma_1 = 1.28$ with a small mass $M \sim 1.5M_{\odot}$, the mass of the inner core formed at the bounce is very small, and as a result, type-III gravitational waves are emitted [34] with the small maximum amplitude as $|\ddot{I}_{zz} - \ddot{I}_{xx}| \sim 30$ cm. On the other hand, for $\Gamma_1 = 1.28$ with a large mass $M \sim 2.5M_{\odot}$, the mass of the inner core can be sufficiently large due to its strong self-gravity. As a result, type-I gravitational waves are emitted and the amplitude of gravitational waves is significantly increased.

An interesting finding in gravitational waveforms for the larger-mass model is that the first spike in the ring-down phase emitted just after the strong negative spike at the bounce decreases as the mass of the iron core increases (see Fig. 24). This spike is associated with the outward motion of the inner core and usually positive for the smaller-mass models (such as models of $M \approx 1.5M_{\odot}$ studied in [29,34,36]). For models of larger mass such as studied in this paper, on the other hand, the post-bounce first spike becomes negative due to suppression of the outward oscillation by the infalling matter. The suppression is larger, in particular, in the direction of the rotational axis because of the absence of the centrifugal force. This decreases the oscillation amplitude to be negative.

Gravitational waveforms for models D5b and D5c are compared to see the dependence on ρ_{nuc} in Fig. 25. It shows that differences in the dynamics associated with the difference in the value of ρ_{nuc} are reflected in gravitational waveforms. For example, the amplitude at the bounce for D5c is smaller than that for D5b. This is because the central density at the bounce is smaller for D5c, and accordingly, the characteristic time scale is longer. On the other hand, the amplitude of the post-bounce

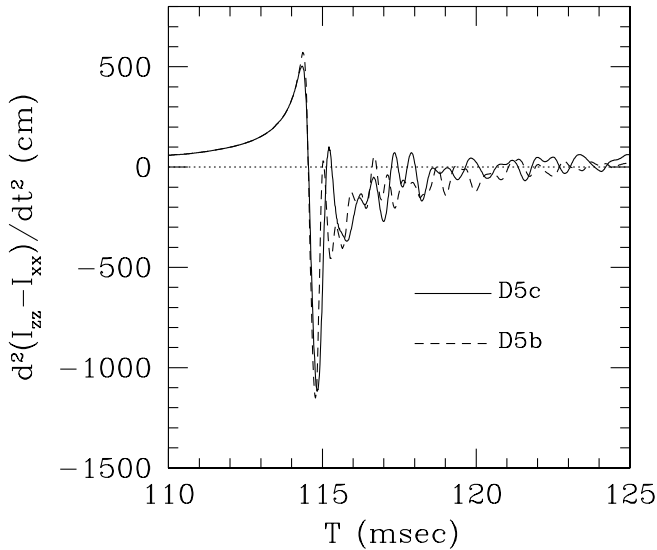


FIG. 25. The same as Fig. 21 but for models D5b (dashed curve) and D5c (solid curve).

first spike is larger for D5c. This is because the amplitude of oscillation of the inner core is larger for D5c as described in Sec. IV B 3.

Before closing this subsection, we comment on the frequency of gravitational waves emitted in the case of black hole formation. After the formation of a black hole, the ambient matter falls into it. As a result, the so-called quasinormal modes (e.g. [82]) of the black hole will be excited and gravitational waves associated with the space-time oscillation will be emitted. According to Echeverria [83], semiempirical expression for the real part of the quasinormal mode frequency for $l = 2$ is given by

$$f \approx 12 \left(\frac{M}{M_\odot} \right)^{-1} \left(\frac{F(q)}{37/100} \right) \text{ kHz}, \quad (42)$$

where

$$F(q) \approx 1 - \frac{63}{100} (1 - q)^{3/10}. \quad (43)$$

Equation (42) indicates that the frequency of gravitational waves associated with the quasinormal mode is ~ 7.5 kHz for models D3 and F5 for which the mass and spin parameter of the formed black hole are predicted to be $M \approx 2.3\text{--}2.4M_\odot$ and $q \approx 0.7$ (see Sec. IV C). This value is far out of the best-sensitive frequency range for detection of laser interferometric gravitational wave detector [84].

In reality, the mass of black hole will significantly increase in a longterm evolution since the matter outside the iron core will fall into a black hole. After such accretion, the frequency of the quasinormal mode will be decreased significantly. Gravitational waves emitted from a high-mass black hole $M \gtrsim 20M_\odot$ may have an appropriate frequency for detection by the laser interferometric detectors.

2. Energy power spectra

In Fig. 26, we show the energy power spectra of gravitational waves with a mode of $l = 2$ and $m = 0$ for selected models. For all the models, the maximum values of the spectra are located at $f_{\text{peak}} \approx 1\text{--}2$ kHz, which are consistent with the typical bounce time intervals of these models $\sim 0.5\text{--}1$ ms. The value $f_{\text{peak}} \approx 1\text{--}2$ kHz is by a factor of ~ 2 larger than the previous Newtonian results [29,33]. This reflects the features in the dynamics of the collapse that the central density and compactness of the inner core at the bounce in general relativity are larger than those in the Newtonian results due to the stronger attraction force [34]. The peak frequency is slightly larger than that found by Dimmelmeier *et al.* [34]. This is due to the fact that the mass of the iron core adopted in this work is larger than theirs. For $f \gtrsim 2$ kHz, the spectra decline steeply for all the models. This feature is consistent with that in [33,34].

The spectrum for model D5a [see Fig. 26(a)] is rather broad for a low frequency region ($100 \leq f \leq 1000$ Hz) and flatter than those for other models. Such characteristic spectrum results from the nature of the bipolar explosion. For models D5b–D5d [see Fig. 26(b)–26(d)], on the other hand, the spectra are quite similar to that of typical type-I burstlike gravitational waves [26,29,34]. In these cases, a few sharp peaks appear at the frequency between 1 and 2 kHz. In Fig. 26(b), the energy power spectrum for smaller-mass model A5b is shown for comparison with the spectrum for model D5b. It is found that the shape of the spectra for these two models is quite similar although the height of the peak for model A5b is smaller than that for model D5b and the peak slightly shifts to the low frequency side due to the fact that the mass is smaller.

The spectrum for model D5c [see Fig. 26(c)] is similar to that for model D5b except for slight shift of the spectrum to low frequency side. The smaller peak frequency results from the fact that the central density at the bounce and of the formed protoneutron star for model D5c is smaller than those for model D5b (cf. Figures 3 and 4), and hence, the dynamical time scale is longer. In Fig. 26(c), the energy power spectrum for model D2c is also shown to see dependence of the spectra on the angular momentum of the progenitor. The magnitude of the spectrum for model D2c is overall smaller than that for model D5c, indicating the magnitude of the angular momentum plays an important role for amplifying the gravitational wave amplitude. Also found is that the peak at $f \approx 1$ kHz is dominant for model D2c. This indicates that for the smaller value of the angular momentum, a single mode is dominantly excited. The reason is likely to be that the degree of deformation of the inner core is smaller for the smaller value of the angular momentum, and hence, the fundamental quadrupole mode of the formed protoneutron star is dominantly excited.

The spectrum for model D5d [see Fig. 26(d)] has a more complicated shape than those for models D5b and D5c. In

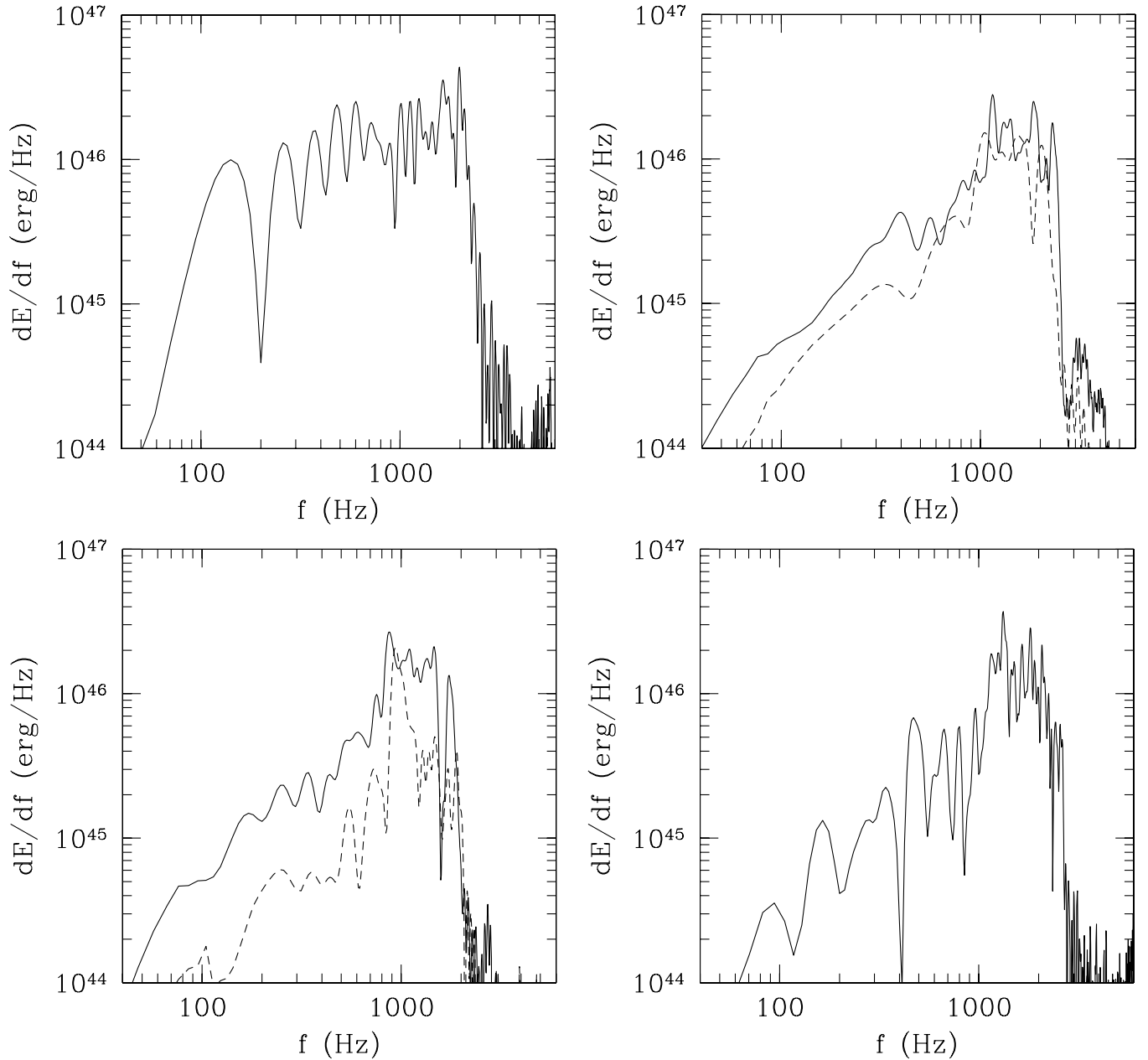


FIG. 26. The energy power spectra of $\tilde{A}_2(f)$ mode for (a) model D5a, (b) models D5b (solid curve) and A5b (dashed curve), (c) models D5c (solid curve) and D2c (dashed curve), and (d) model D5d. Note that gravitational waveforms for models D5a, D5b, D5c, and D5d are shown in Figs. 21, 22, 25, and 23, respectively.

particular, several small peaks in the low frequency region are found between 100 and 1000 kHz, indicating that several oscillation modes are excited simultaneously. This reflects the manner on the generation of the shocks at the surface of the protoneutron star in the equation of state d: As mentioned in Sec. IV D, the mass of the formed protoneutron star is initially small with the equation of state “d,” and as a result, the accretion of the matter which gradually falls from the shock layer subsequently proceeds. The accreted matter intermittently hits the protoneutron star and excites its oscillation modes in a complicated

manner. As a result, gravitational waves of several characteristic oscillation frequencies are generated.

V. SUMMARY

We performed fully general relativistic simulations for black hole formation through the collapse of rotating iron cores on assumption of the axial symmetry for a wide variety of the mass, the angular momentum, the velocity profile, and the equation of state. To systematically study the dependence of the threshold mass for the prompt black

hole formation on the equations of state, we adopt a parametric equation of state [29,34,51]. We choose the parameters so that the maximum mass of the cold spherical neutron star becomes $\approx 1.6M_{\odot}$. The rotating iron cores before collapse are simply modeled by the rotating $\Gamma = 4/3$ polytrope in equilibrium. The mass of the iron core is set to be $\approx 2.0\text{--}3.0M_{\odot}$. The amount of rotational kinetic energy of the core is changed in a wide range from $T_{\text{rot}}/W = 0$ to ≈ 0.009 .

We have found that the threshold mass for the prompt black hole formation depends sensitively on the angular momentum, the rotational velocity profile of the initial core, and the equations of state. The dependence of the threshold mass on these elements can be summarized as follows: (i) The thermal pressure generated by shocks increases the threshold mass by 20–40%. The magnitude of this factor depends on the adopted equation of state: (ii) With the increase of the spin parameter q , the threshold mass increased by $\sim 25q^2\%$ for the case that the progenitor is rigidly rotating; (iii) Effect of differential rotation further increases the threshold mass, since the centrifugal force around the central region can be efficiently increased; (iv) The threshold mass depends sensitively on the equations of state since the dynamics of the collapse does. For the smaller value of $|\Gamma_1 - 4/3|$ and for the larger value of ρ_{nuc} , prompt black hole formation becomes more liable since the mass of the inner core at the bounce is larger for such equations of state.

About the dynamics of the collapse, we have found the following features: (i) if Γ_1 is close to $4/3$, the collapse proceeds in an approximately homologous manner, and thus, the most part of the iron core collapses nearly simultaneously. This implies that the mass of the inner core formed at the bounce is larger for the smaller value of $|\Gamma_1 - 4/3|$, that helps prompt black hole formation as mentioned above. In the case that the mass of the progenitor is not large enough, not a black hole but a protoneutron star is formed. Since the mass of the inner core is larger for the small value of $|\Gamma_1 - 4/3|$, the inner core shrinks more significantly resulting in a larger degree of the aspherical deformation and in a significant spin-up. As a result, the shape of the shock is highly aspherical and the explosion proceeds in a strongly bipolar manner if the progenitor is rapidly rotating as $T_{\text{rot}}/W \approx 0.009$ (see Sec. IV D 1): (ii) For $\Gamma_1 \lesssim 1.3$, the collapse does not proceed in the homologous manner. Instead, only the central region rapidly collapses and forms the inner core of a small mass at the bounce. As a result, prompt black hole formation is less liable. For the cases of protoneutron star formation, the aspherical deformation of the inner core is not very remarkable since its mass at the bounce is not sufficiently large, and hence, the effect of the centrifugal force is not very important. Consequently, the shape of the shock is only slightly aspherical even when the progenitor is rapidly rotating (see Sec. IV D 1): (iii) For the equation of state

“c” in which the value of ρ_{nuc} is smaller than that for others, the pressure for $10^{14} \text{ g/cm}^3 \leq \rho \leq 2 \times 10^{15} \text{ g/cm}^3$ is larger than that for the equations of state “b” and “d.” As a result, strength of the shocks formed at the bounce is enhanced, and therefore, black holes are less liable to be formed.

Gravitational waveforms are approximately computed in terms of a quadrupole formula [55]. It is found that the amplitude of gravitational waves at the bounce increases monotonically as the mass and angular momentum of the iron core increase as far as $M \lesssim 2.5M_{\odot}$. In contrast to the previous results (e.g., [28]), we do not find any tendency that the maximum amplitude saturates with the increase of the angular momentum for a given mass. This is due to the fact that the general relativistic gravity is strong enough for the inner core to form a compact protoneutron star overcoming the centrifugal force in the present choice of the spin parameter ($0 \leq q \leq 1$) for the rigidly rotating case.

Gravitational waveforms depend sensitively on the equation of state. For models with the equations of state “b,” “c,” and “d,” the so-called type-I gravitational waves are emitted even with the mass $M \sim 2\text{--}2.5M_{\odot}$ as in the case of mass $M \approx 1.4\text{--}1.5M_{\odot}$ which is studied in the previous papers [34,36]. With the increase of the mass, the amplitude and the frequency of gravitational waves become higher. Thus, the difference is only quantitative for the equations of state “b” and “c.” A point worthy to note is that type-I gravitational waves are emitted for $M \geq 2M_{\odot}$ even for the equation of state “d” (with $\Gamma_1 = 1.28$). For $M \approx 1.5M_{\odot}$, type-III gravitational waves are emitted for such small value of Γ_1 since the mass of the inner core is very small at the bounce. However, in the higher-mass case with $M \geq 2M_{\odot}$, the mass of the inner core formed at the bounce is large enough to emit type-I gravitational waves. Gravitational waveforms in the collapse of rapidly rotating iron core with the equation of state a in which $\Gamma_1 = 1.32$ are qualitatively different from others. The reason is that in such case, an outstanding bipolar explosion is induced along the rotational axis and gravitational waves associated with such extreme explosion and with the resulting oscillation of the inner core in the direction of the rotational axis are emitted. Because of this change, the shape of the energy power spectrum is also qualitatively different from others.

In this paper, we assume that the collapse proceeds in the axisymmetric manner. However, the rotating iron core may be dynamically unstable against the nonaxisymmetric deformation during the collapse if the spin is increased significantly during the collapse, and as a result, the value of T_{rot}/W exceeds a critical value ~ 0.27 . To determine the criterion for the onset of nonaxisymmetric instabilities, we performed three-dimensional simulation for the iron core collapse in a companion paper [38], which shows that in the collapse for rigidly rotating models, the value of T_{rot}/W for the formed protoneutron star is far below the critical

value for the onset of the dynamical instabilities, and the nonaxisymmetric instability does not set in. Therefore, the assumption of the axial symmetry adopted in this paper is justified.

Finally, we mention a direction of our next study. In this paper, we have clarified a criterion for prompt black hole formation in the iron core collapse adopting the parametric equations of state as a first step. We have shown that the dynamics of the collapse and the criterion for the black hole formation depend sensitively on the equations of state. To obtain more realistic outputs that will be in nature, in the next step, it is necessary to adopt more realistic equations of state. We plan to perform such realistic simulations adopting a realistic equation of state [53] in the fully general relativistic framework.

ACKNOWLEDGMENTS

Numerical computations were performed on the FACOM VPP5000 machine in the data processing center of National Astronomical Observatory of Japan and NEC SX-6 in the data processing center of ISAS in JAXA. This work is supported by JSPS Research Grant for Young Scientists (No. 1611308) and by Monbukagakusho Grant (Nos. 15037204, 15740142, and 16029202).

APPENDIX: COMPARISON WITH REALISTIC EQUATION OF STATE

In this appendix, we compare the parametric equation of state (PEOS) adopted in this paper (see Sec. II B) with a

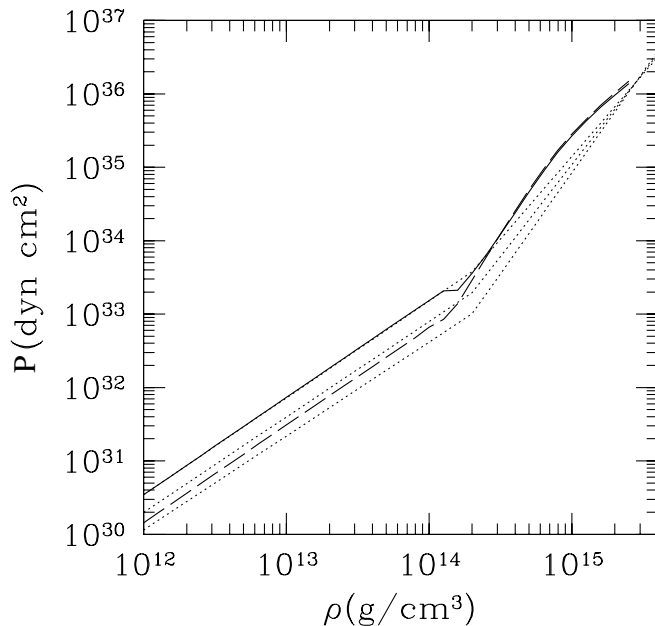


FIG. 27. The pressure, P , as a function of the density, ρ , for the realistic equation of state at zero temperature. The solid curve corresponds to the case $Y_e = 0.5$ and the long dashed to $Y_e = 0.2$. The three dotted curves denote the cold equations of state with the parameters listed in Table I.

realistic equation of state proposed by Shen *et al.* [53] (REOS). In Fig. 27, we show relations between the pressure and the density of REOS at zero temperature (adding the degenerate electron pressure) together with those of PEOS. Since REOS depends on Y_e , we consider the two values $Y_e = 0.5$ and 0.2 . The P - ρ relations of REOS and PEOS shows a good agreement, in particular, in the subnuclear density. In the supranuclear density, on the other hand, difference between the two equations of state becomes outstanding: The REOS is stiffer than PEOS (see discussion about Γ_2 below). This fact leads to the larger maximum mass of the spherical cold neutron star for REOS. Indeed, the maximum ADM mass is $\approx 2.2M_\odot$ [53], much larger than that for PEOS ($\approx 1.6M_\odot$).

We first consider the validity of the adiabatic index of PEOS at subnuclear density Γ_1 . The adiabatic index Γ_1 includes the effect of the electron capture. This implies that it corresponds to an average value $\langle \Gamma_M \rangle$ of the “effective” adiabatic index Γ_M [26,85] which describes the change of the pressure along a collapse trajectory of a given mass element:

$$\Gamma_M = \left. \frac{\partial \log P}{\partial \log \rho} \right|_{s, Y_e} + \left. \frac{\partial \log P}{\partial Y_e} \right|_{\rho, s} \frac{\delta Y_e}{\delta \log \rho} \Big|_M + \left. \frac{\partial \log P}{\partial S} \right|_{\rho, Y_e} \frac{\delta S}{\delta \log \rho} \Big|_M, \quad (\text{A1})$$

where $\delta S = 0$ at zero temperature. The crucial quantity for the dynamical behavior of the core is this effective adiabatic index Γ_M [26,86].

On the other hand, the P - ρ relations for REOS in Fig. 27 do not include the effect of the electron capture. Since Y_e decreases during the collapse due to the electron capture, the P - ρ relation will shift toward that of the smaller Y_e . If the electron capture rate is small, the effective adiabatic index will be close to $4/3$, while the rate is large, the index will deviate from $4/3$.

A plausible value of $\langle \Gamma_M \rangle$ for REOS in subnuclear density would be estimated as follows. First, previous studies suggest that the initial value of Y_e is ≈ 0.42 and $-0.11 \leq \delta Y_e \leq -0.04$ during the collapse [13,87]. Assuming these values and $\delta \log \rho \approx 4$, the average value of $(\delta Y_e / \delta \log \rho)|_M$ is $-0.01 - -0.0275$. On the other hand, the value of $(\partial \log P / \partial Y_e)|_{\rho, s}$ of REOS is $\approx 1.4 - 1.9$ for $10^8 \leq \rho \leq 10^{14}$ and $0.31 \leq Y_e \leq 0.42$, and its averaged value is ≈ 1.6 . Thus, the average value for REOS is $1.29 \leq \langle \Gamma_M \rangle \leq 1.32$ depending the electron capture rate. Therefore, the range $1.28 \leq \Gamma_1 \leq 1.32$ adopted in this paper would be reasonable.

Then, let us consider the adiabatic index Γ_2 at supranuclear density. The adiabatic index of REOS at supranuclear density is larger ($\Gamma \approx 3$) than that of PEOS ($2.25 \leq \Gamma_2 \leq 2.75$). This is due to a relatively larger value of incompressibility of the REOS: $K_s = 281$ MeV [53]. Although the real value of K_s is uncertain at current status, a recent study [88] reported that a plausible range of the

value of K_s is ≈ 220 – 270 MeV. Therefore, the adiabatic index can be much smaller for a smaller value of K_s . For example, the adiabatic index is ≈ 2.2 around the nuclear matter density for a realistic equation of state by Lattimer and Swesty with $K_s = 220$ MeV [52]. Thus, the range

$2.25 \leq \Gamma_2 \leq 2.75$ adopted in this paper may be a plausible choice.

In summary, we conclude that the parameter range adopted in the present paper is not far from predictions and suggestion of realistic equations of state.

-
- [1] M. J. Rees, in *The Future of Theoretical Physics and Cosmology: Celebrating Stephen Hawking's 60th Birthday*, edited by G. W. Gibbons *et al.* (Cambridge University Press, Cambridge, England, 2003), p. 217; astro-ph/0401365.
- [2] J. E. McClintock and R. A. Remillard, in *Compact Stellar X-ray Sources*, edited by W. H. G. Lewin and van der Klis (Cambridge University Press, Cambridge, England, 2005); astro-ph/0306213 (to be published).
- [3] T. Piran, Rev. Mod. Phys. **76**, 1143 (2005); in *Proceedings of the 16th International Conference on General Relativity and Gravitation*, edited by N. T. Bishop and S. D. Maharaj (World Scientific, Singapore, 2002), p. 259, and references therein.
- [4] J. van Paradijs *et al.*, Nature (London) **386**, 686 (1997); M. R. Metzger *et al.*, Nature (London) **387**, 878 (1997); S. R. Kulkarni *et al.*, Nature (London) **393**, 35 (1998).
- [5] T. J. Galama *et al.*, Nature (London) **395**, 670 (1998); K. Z. Stanek *et al.*, Astrophys. J. Lett. **591**, L17 (2003); J. Hjorth *et al.*, Nature (London) **423**, 847 (2003); K. S. Kawabata *et al.*, Astrophys. J. Lett. **593**, L19 (2003).
- [6] L. Wang and J. C. Wheeler, Astrophys. J. Lett. **504**, L87 (1998);
- [7] S. E. Woosley, Astrophys. J. **405**, 273 (1993).
- [8] B. Paczyński, Astrophys. J. Lett. **494**, L45 (1998).
- [9] A. I. MacFadyen and S. E. Woosley, Astrophys. J. **524**, 262 (1999).
- [10] M. Shibata, Astrophys. J. **605**, 350 (2004).
- [11] S. L. Shapiro, Astrophys. J. **610**, 913 (2004).
- [12] Y. Sekiguchi and M. Shibata, Phys. Rev. D **70**, 084005 (2004).
- [13] S. L. Shapiro and S. A. Teukolsky, *Black Holes, White Dwarfs, and Neutron Stars* (Wiley Interscience, New York, 1983).
- [14] S. E. Woosley, A. Heger, and T. A. Weaver, Rev. Mod. Phys. **74**, 1015 (2002).
- [15] I. Fukuda, Publ. Astron. Soc. Pac. **94**, 271 (1982).
- [16] T. Nakamura, Prog. Theor. Phys. **65**, 1876 (1981); **70**, 1144 (1983).
- [17] T. Nakamura, K. Oohara, and Y. Kojima, Prog. Theor. Phys. Suppl. **90**, 1 (1987).
- [18] R. F. Stark and T. Piran, Phys. Rev. Lett. **55**, 891 (1985); T. Piran and R. F. Stark in *Dynamical Spacetimes and Numerical Relativity*, edited by J. M. Centrella (Cambridge University Press, Cambridge, England, 1986).
- [19] M. Shibata and S. L. Shapiro, Astrophys. J. **572**, L39 (2002).
- [20] M. Shibata, T. W. Baumgarte, S. L. Shapiro, Phys. Rev. D **61**, 044012 (2000).
- [21] M. Shibata, Astrophys. J. **595**, 992 (2003).
- [22] L. Baiotti, I. Hawke, P. J. Montero, F. Löffler, L. Rezzolla, N. Stergioulas, J. A. Font, and E. Seidel, Phys. Rev. D **71**, 024035 (2005).
- [23] M. D. Duez, S. L. Shapiro, and H.-J. Yo, Phys. Rev. D **69**, 104016 (2004); M. D. Duez, Y. T. Liu, S. L. Shapiro, and B. C. Stephens, Phys. Rev. D **69**, 104030 (2004).
- [24] E. Müller and W. Hillebrandt, Astron. Astrophys. **103**, 358 (1981); E. Müller, Astron. Astrophys. **114**, 53 (1982).
- [25] L. S. Finn and C. R. Evans, Astrophys. J. **351**, 588 (1990).
- [26] R. Mönchmeyer, G. Schäfer, E. Müller, and R. E. Kates, Astron. Astrophys. **264**, 417 (1991).
- [27] S. Bonazzola and J. A. Marck, Astron. Astrophys. **267**, 623 (1993).
- [28] S. Yamada and K. Sato, Astrophys. J. **434**, 268 (1994); **450**, 245 (1995).
- [29] T. Zwerger and E. Müller, Astron. Astrophys. **320**, 209 (1997).
- [30] M. Rampp, E. Müller, and M. Ruffert, Astron. Astrophys. **332**, 969 (1998).
- [31] C. L. Fryer and A. Heger, Astrophys. J. **541**, 1033 (2000); C. Fryer, D. Holz, and S. Hughes, Astrophys. J. **565**, 430 (2002).
- [32] K. Kotake, S. Yamada, and K. Sato, Phys. Rev. D, **68**, 044023, (2003); K. Kotake, S. Yamada, K. Sato, K. Sumiyoshi, H. Ono, and H. Suzuki, Phys. Rev. D **69**, 124004 (2004).
- [33] C. D. Ott, A. Burrows, E. Livne, and R. Walder, Astrophys. J. **600**, 834 (2004).
- [34] H. Dimmelmeier, J. A. Font, and E. Müller, Astron. Astrophys. **388**, 917 (2002); **393**, 523 (2002).
- [35] J. R. Wilson and G. J. Mathews, Phys. Rev. Lett. **75**, 4161 (1995).
- [36] M. Shibata and Y. Sekiguchi, Phys. Rev. D **69**, 084024 (2004).
- [37] F. Siebel, J. A. Font, E. Müller, and P. Papadopoulos, Phys. Rev. D **67**, 124018 (2003).
- [38] M. Shibata and Y. Sekiguchi, Phys. Rev. D **71**, 024014 (2005).
- [39] M. Shibata, Phys. Rev. D **67**, 024033 (2003).
- [40] M. Shibata, Prog. Theor. Phys. **101**, 1199 (1999); Phys. Rev. D **60**, 104052 (1999).
- [41] M. Shibata and K. Uryū, Phys. Rev. D **61**, 064001 (2000); Prog. Theor. Phys. **107**, 265 (2002).
- [42] M. Shibata, K. Taniguchi, and K. Uryū, Phys. Rev. D **68**, 084020 (2003).
- [43] M. Shibata and T. Nakamura, Phys. Rev. D **52**, 5428 (1995).
- [44] M. Shibata, Prog. Theor. Phys. **104**, 325 (2000).

- [45] M. Alcubierre, S. Brandt, B. Brügmann, D. Holz, E. Seidel, R. Takahashi, and J. Thornburg, *Int. J. Mod. Phys. D* **10**, 273 (2001).
- [46] J. A. Font, *Living Rev. Relativity* **6**, 4 (2003); F. Banyuls, J. A. Font, J.-Ma. Ibáñez, J. M. Martí, and J. A. Miralles, *Astrophys. J.* **476**, 221 (1997).
- [47] T. W. Baumgarte, S. L. Shapiro, and M. Shibata, *Astrophys. J.* **528**, L29 (2000).
- [48] M. Alcubierre, B. Brügmann, D. Pollney, E. Seidel, and R. Takahashi, *Phys. Rev. D* **64**, 061501(R) (2001); L. Lindblom and M. A. Scheel, *Phys. Rev. D* **67**, 124005 (2003).
- [49] M. Shibata, *Phys. Rev. D* **55**, 2002 (1997).
- [50] J. W. York, Jr. and T. Piran, in *Spacetime and Geometry: The Alfred Schild Lectures*, edited by R. A. Matzner and L. C. Shepley (University of Texas Press, Texas, 1982).
- [51] H.-T. Janka, T. Zwerger, and R. Mönchmeyer, *Astron. Astrophys.* **268**, 360 (1993).
- [52] J. M. Lattimer and F. D. Swesty, *Nucl. Phys.* **A535**, 331 (1991).
- [53] H. Shen, H. Toki, K. Oyamatsu, and K. Sumiyoshi, *Nucl. Phys.* **A637**, 435 (1998); H. Shen, H. Toki, K. Oyamatsu, and K. Sumiyoshi, *Prog. Theor. Phys.* **100**, 1013 (1998).
- [54] I. H. Stairs, *Science* **304**, 547 (2004).
- [55] M. Shibata and Y. Sekiguchi, *Phys. Rev. D* **68**, 104020 (2003).
- [56] K. S. Thorne, in *300 Years of Gravitation*, edited by S. W. Hawking and W. Israel (Cambridge University Press, Cambridge, 1987).
- [57] X. Zhuge, J. M. Centrella, and S. L. W. McMillan, *Phys. Rev. D* **50**, 6247 (1994).
- [58] J. J. Eldridge and C. A. Tout, *Mon. Not. R. Astron. Soc.* **353**, 87 (2004).
- [59] H. Umeda and K. Nomoto, (unpublished).
- [60] R. Hirschi, G. Meynet, and A. Maeder, *Astron. Astrophys.* **425**, 649 (2004).
- [61] A. Heger, N. Langer, and S. E. Woosley, *Astrophys. J.* **528**, 368 (2000).
- [62] C. L. Fryer, *Astrophys. J.* **522**, 413 (1999).
- [63] A. Heger, C. L. Fryer, S. E. Woosley, N. Langer, and D. H. Hartmann, *Astrophys. J.* **591**, 288 (2003).
- [64] See, e.g., H. Komatsu, Y. Eriguchi, and I. Hachisu, *Mon. Not. R. Astron. Soc.* **237**, 355 (1989); **239**, 153 (1989).
- [65] N. Stergioulas, *Living Rev. Relativity* **6**, 3 (2003).
- [66] J. L. Friedman, J. R. Ipser, and L. Parker, *Astrophys. J.* **304**, 115 (1986).
- [67] G. B. Cook, S. L. Shapiro, and S. A. Teukolsky, *Astrophys. J.* **398**, 203 (1992).
- [68] S. Karino and Y. Eriguchi, *Astrophys. J.* **592**, 1119 (2003).
- [69] M. Shibata, S. Karino, and Y. Eriguchi, *Mon. Not. R. Astron. Soc.* **334**, L27 (2002); **343**, 619 (2003).
- [70] K. A. Van Riper, *Astrophys. J.* **257**, 793 (1982).
- [71] E.g., A. Burrows and J. M. Lattimer, *Astrophys. J.* **307**, 178 (1986).
- [72] J. M. Bardeen, W. H. Press, and S. A. Teukolsky, *Astrophys. J.* **178**, 347 (1972).
- [73] M. Alcubierre and B. Brügmann, *Phys. Rev. D* **63**, 104006 (2001).
- [74] K. Iwamoto *et al.*, *Nature (London)* **395**, 672 (1998).
- [75] K. Maeda, T. Nakamura, K. Nomoto, P. Mazzali, F. Patat, and I. Hachisu, *Astrophys. J.* **565**, 405 (2002); K. Maeda, P. Mazzali, J. Deng, K. Nomoto, Y. Yoshii, H. Tomita, and Y. Kobayashi, *Astrophys. J.* **593**, 931 (2003).
- [76] L. Wang, A. Howell, P. Höflich, and J. C. Wheeler, *Astrophys. J.* **550**, 1030 (2001).
- [77] K. Nomoto, K. Maeda, P. Mazzali, H. Umeda, J. Deng, and K. Iwamoto, in *Stellar Collapse*, edited by C. L. Fryer (Kluwer Academic, Dordrecht, 2004); astro-ph/0308136.
- [78] M. Shibata, T. W. Baumgarte, and S. L. Shapiro, *Astrophys. J.* **542**, 453 (2000).
- [79] S. Karino and Y. Eriguchi, *Astrophys. J.* **578**, 413 (2002).
- [80] N. Stergioulas and J. L. Friedman, *Astrophys. J.* **492**, 301 (1998); S. Morsink, N. Stergioulas, and S. Blattning, *Astrophys. J.* **510**, 854 (1999).
- [81] S. Bonazzola, J. Friebe, and E. Gourgoulhon, *Astron. Astrophys.* **331**, 280 (1998).
- [82] K. D. Kokkotas and B. G. Schmidt, *Living Rev. Relativity* **2**, 2 (1999).
- [83] F. Echeverria, *Phys. Rev. D* **40**, 3194 (1989).
- [84] C. Cutler and K. S. Thorne, in *Proceedings of the 16th International Conference on General Relativity and Gravitation*, edited by N. T. Bishop and S. D. Maharaj (World Scientific, Singapore, 2002), p. 72, and references therein.
- [85] J. Cooperstein and E. A. Baron, in *Supernovae*, edited by A. G. Petschek (Springer-Verlag, New York, 1990).
- [86] K. A. Van Riper and J. M. Lattimer, *Astrophys. J.* **249**, 270 (1981).
- [87] H. A. Bethe, *Rev. Mod. Phys.* **62**, 801 (1990).
- [88] G. Colò and N. Van Giai, *Nucl. Phys.* **A731**, 15 (2004).